INVESTIGATING THE EFFECT OF CATALYSTS IN SODIUM-OXYGEN BATTERIES

A THESIS SUBMITTED TO
THE GRADUATE SCHOOL OF ENGINEERING AND SCIENCE
OF BILKENT UNIVERSITY
IN PARTIAL FULFILLMENT OF THE REQUIREMENTS FOR
THE DEGREE OF
MASTER OF SCIENCE
IN
MATERIALS SCIENCE AND NANOTECHNOLOGY

By
Mohammad Fathi Tovini
November 2017

INVESTIGATING THE EFFECT OF CATALYSTS IN SODIUM-OXYGEN BATTERIES

By Mohammad Fathi Tovini

November 2017

We certify that we have read this thesis and that in our opinion it is fully adequate, in scope and in quality, as a thesis for the degree of Master of Science.

Eda Yılmaz(Advisor)

Damla Eroğlu Pala

Burak Ülgüt

Approved for the Graduate School of Engineering and Science:

Ezhan Karaşan
Director of the Graduate School

ABSTRACT

INVESTIGATING THE EFFECT OF CATALYSTS IN SODIUM-OXYGEN BATTERIES

Mohammad Fathi Tovini
M.S. in Materials Science and Nanotechnology
Advisor: Eda Yılmaz
November 2017

The unique electrochemical and chemical features of sodium oxygen (Na-O_2) batteries distinguish them from the lithium-oxygen (Li-O_2) batteries. NaO_2, which is the main discharge product, is unstable in the cell environment and its dissolution in the electrolyte triggers side products formation and charging potential increment. In the first part of this thesis, RuO_2 nanoparticles (NPs) dispersed on carbon nanotubes (CNTs) are used as a catalyst for Na-O_2 batteries to elucidate the effect of catalyst on this complex electrochemical system. RuO_2/CNT contributes to the formation of a poorly crystalline and coating like NaO_2 structure during oxygen reduction reaction (ORR) which is drastically different from the conventional micron sized cubic NaO_2 crystals deposited on CNT. Our findings demonstrate a competition among NaO_2 and side products decompositions for RuO_2/CNT during oxygen evolution reaction (OER). We believe that this is due to the lower stability of coating like NaO_2 because of its non-crystalline nature and high electrode/electrolyte contact area. Although RuO_2/CNT catalyzes the decomposition of side products at a lower potential (3.66 V) compared to CNT (4.03 V), it cannot actively contribute to the main electrochemical reaction of the cell during OER ($NaO_2 \longrightarrow Na^+ + O_2 + e^-$) due to the fast chemical decomposition of film NaO_2 to side products. Even though the long term effect of RuO_2 catalyst during cycling and resting tests seems to be positive in terms of lower overpotential, no benefits of catalyst is observed for stability and efficiency of the cell for the first cycles. Therefore, tuning the morphology and crystallinity of NaO_2 by catalyst is detrimental for Na-O_2 cell performance and it should be taken into account for the future applications.

In the second part of this thesis, a 3D RuO_2/Mn_2O_3/carbon nanofiber (CNF) composite has been prepared as a bi-functional electrocatalyst towards oxygen reduction reaction (ORR) and oxygen evolution reaction (OER) in Na-O_2 batteries. RuO_2/Mn_2O_3/CNF exhibited higher specific capacity (9352 mAh.g_{carbon}^{-1}) than

CNF (1395 mAh.g_{carbon}^{-1}), Mn_2O_3/CNF (3108 mAh.g_{carbon}^{-1}) and RuO_2/CNF (4859 mAh.g_{carbon}^{-1}), which is believed to be due to its higher active surface area than its counterparts and its unique morphology. Taking the benefit of RuO_2 and Mn_2O_3 synergistic effect, the decomposition of inevitable side products at the end of charge occurs at 3.838 V vs. Na/Na^+ by using RuO_2/Mn_2O_3/CNF, which is 388 mV more cathodic compared with CNF.

Keywords: Catalyst, Na-O_2 battery, NaO_2 dissolution, oxygen evolution reaction, oxygen reduction reaction, side product.

ÖZET

SODYUM-OKSIJEN PILLERDE KATALIZÖRLERIN ETKILERININ ARAŞTIRILMASI

Mohammad Fathi Tovini
Malzeme Bilimi ve Nanoteknoloji, Yüksek Lisans
Tez Danışmanı: Eda Yılmaz
Kasım 2017

Sodyum-oksijen (Na-O_2) pillerin şsiz elektrokimyasal ve kimyasal özellikleri onları lityum-oksijen (Li-O_2) pillerden ayrı kılmaktadır. Ana deşarj ürünü olan NaO_2, hücre ortamında kararsızdır ve bu ürünün elektrolit içerisinde çözünmesi yan ürün oluşumunu tetiklemekte ve şarj potansiyelinin artmasına sebep olmaktadır. Bu tezin ilk kısmında, karbon nanotüpler (KNT) üzerinde dağıtılmış RuO_2 nanoparçacıkları Na-O_2 piller için katalizör olarak kullanılmış ve katalizörün bu kompleks sistem üzerindeki etkileri aydınlatılmaya çalışılmıştır. RuO_2/KNT katotların oksijen indirgenme reaksiyonu (ORR) sırasında sadece KNT katotları kullanıldığı zaman oluşan mikron boyuttaki kübik NaO_2 kristalleri yerine, düşük kristalin özellikli ve kaplama şekilde NaO_2 yapısı oluşumunu sağladıkları gözlemlenmiştir. Bulgularımız bizlere oksijen yükseltgeme reaksiyonu (OER) sırasında NaO_2 ve yan ürün parçalanmasş arasında bir yarışın söz konusu olduğunu göstermiştir. Bu durumun amorf yapıdaki ve kaplama şeklinde oluşan NaO_2 ürününün düşük kararlılığının ve yüksek elektrot/elektrolit temas alanının bir neticesi olduğu düşünülmektedir. RuO_2/KNT katotlarının (3.66 V) yan ürünlerin parçalanmasının KNT katotları (4.03 V) ile karşılaştırıldığında katalize ettikleri görülmüş olsa da, bu katotların NaO_2'nin yan ürünlere çok hızlı bir şekilde dönüşmesinden dolayı şarj sırasında oluşan ana reaksiyon olan OER'a ($NaO_2 \longrightarrow Na^+ + O_2 + e^-$) aktif olarak katkı sağlayamadıkları görülmüştür. Her ne kadar RuO_2 katalizörlerin uzun vadede çevrim ve dinlenme işlemlerinde hücre yüksek gerilimini düşürme üzerinde pozitif etkisi olduğu söylenebilir olsa da katalizörün ilk çevrimlerde hücre kararlılığına ve verimine bir faydasıı olmadığı gözlemlenmiştir. Bu açıdan bakıldığında NaO_2'nin morfolojisinin ve kristal özelliğinin katalizör tarafından ayarlanmasının Na-O_2 hücre performansına zararlı bir etkisinin olduğu ortaya konmuştur ve bunun gelecekteki uygulamalarda göz önünde bulundurulması gerekmektedir.

Tezin ikinci kısmında, 3 boyutlu (3D) RuO_2/Mn_2O_3/karbon nanofiber (KNF) kompozitler hazırlanmış ve bi-fonksiyonel elektrokatalizörler olarak ORR ve OER proseslerine yönelik olarak Na-O_2 pillerde kullanılmışlardır. RuO_2/Mn_2O_3/KNF?nin (9352 mAh.g_{carbon}^{-1}) diğer KNF (1395 mAh.g_{carbon}^{-1}), Mn_2O_3/KNF (3108 mAh.g_{carbon}^{-1}) ve RuO_2/KNF (4859 mAh.g_{carbon}^{-1}) katotlarına göre çok daha yüksek spesifik kapasite sağlamıştır ve bunun sebebinin diğer malzemelerden daha yüksek aktif yüzey alanı ve eşsiz morfolojisi olduğu düşünülmektedir. RuO_2 ve Mn_2O_3 malzemelerinin sağladıkları sinerjistik etki ile şarj sırasında yan ürünlerin parçalanması KNF'ye göre 388 mV daha katodik olan 3.838 V'da gerçekleşmiştir.

Anahtar sözcükler: Katalizör, Na-O_2 Piller, NaO_2 Çözünmesi, Oksijen yükseltgeme reaksiyonu, Oksijen indirgeme reaksiyonu, Yan ürün.

Acknowledgement

Hereby, I want to thank my supervisor Dr. Eda Yilmaz for her inspiring supports during my study and her trust to give me the golden opportunity of being involved in this project. I also thank my adorable friends who are my biggest achievement during this time for being always around. My biggest love to my family at the end...

I acknowledge TUBITAK for the financial support with the project number 115M375.

Contents

List of Figures

Chapter 1

INTRODUCTION

1.1 Energy of Future

Fossil fuels are reported as the source of more than 85% of the world's energy supply during last years. According to experts, this need will grow dramatically in which by 2040, the world's energy demand will increase 56% because of human population growth and the inevitable world wide industrialization. In this way, fossil fuels reservoirs can only satisfy the energy demand only for another 20 years due to the non-renewable nature and restricted sources of fossil fuels. In addition, it has been more than 15 years that the world is concerned about the accelerating rate of green house gas emission, whose the primary source is directly related to the energy production [1].

The alternative renewable energy sources such as hydro, solar, wind and geothermal are developed in order to replace fossil fuels. There are several pros of replacing fossil fuels with renewable energy sources: decrement of green house gases emission to the environment, the creation of new job opportunities in the field of green technologies by developing of diverse energy supplies and etc. Although the sun and wind energies are the most common renewable energy sources for electricity production, the solar energy can be supplied during the daylight and the wind energy is circumstantial. Therefore, these energies are not continuously

supplied when they are needed and consequently, proper energy storage systems are required. Although there are currently many energy storage technologies used in the large scale, they all have some cons including price, capacity, power and mobility. For example, pumped hydro is one of the commonly used techniques in order to store energy, but it requires a large capital expense and proper geographical condition. As a result, energy storage devices with high efficiencies are highly required and batteries are one of the most appropriate candidates for this demand. Batteries can store chemical energy through electrochemical reactions and convert it back into electrical energy and Li batteries are the most applicable ones among the current technologies [2, 3].

1.2 Brief History

The battery was invented by Alessandro Volta in 1800 and since then, it has been the commonly used energy storage device for many applications. Hypothetically, there are two main categories of batteries: primary and secondary (rechargeable) batteries. Primary batteries are designed for only one-time usage and then discarded, but the secondary batteries can be used several times by recharging the battery once it is discharged. There are different types of commercialized secondary batteries like lead acid, nickel metal hydrate and lithium ion (Li-ion) batteries, however, Li-ion batteries got more attention regarding their better performance compared to the other systems. Lithium batteries were firstly introduced by M.S. Whittingham in 1970s and many distinct contributions were made by John B. Goodenough afterward [4, 5]. Since 1991, when Li-ion batteries were firstly commercialized by Sony, many fundamental and practical advances have been achieved in this field and today, these devices attain the highest capacity among the available commercial batteries, which makes them the most proper energy storage systems for diverse applications. However, they suffer from a limited energy density and specific energy (energy per unit volume and unit mass, respectively) for implementation in electric vehicles, even if the theoretical capacity of cathode material is achieved [2]. Accordingly, many efforts have been focused on developing new energy storage technologies beyond Li-ion batteries in

order to overcome these constraints [6]. Metal-O_2 batteries (Li-O_2, Na-O_2 and etc.) are the best candidates in order to their extremely higher energy density compared to Li-ion batteries and their energy storage mechanism is based on the reaction of metals and O2 and the deposition of solid state discharge products on the porous cathode electrode (Figure 1.1) [7].

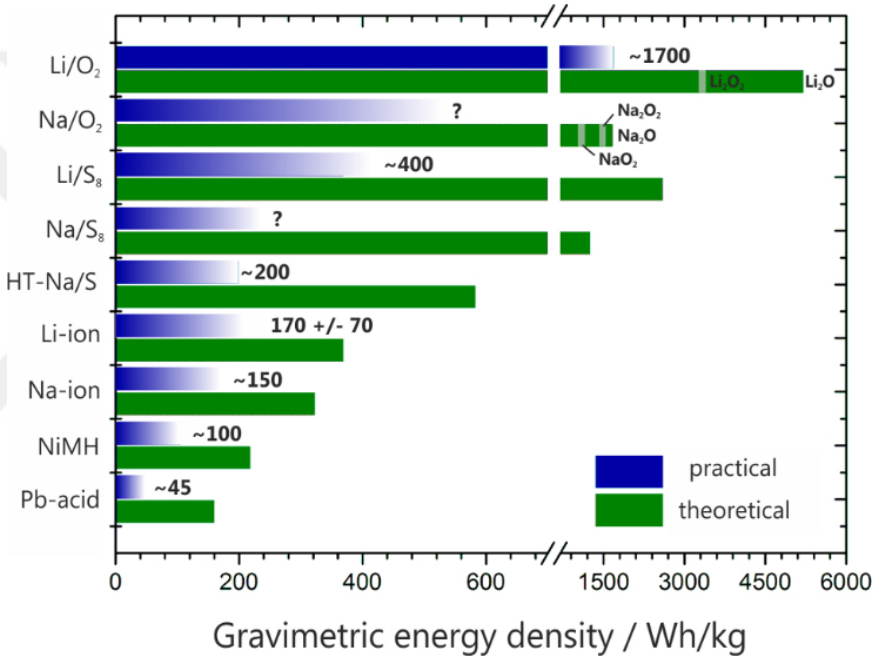

Figure 1.1: Comparison of the energy density of different battery types [8].

The first spark of metal-O_2 batteries was kindled in 1979 by Blurton and Sammels, publishing the first review on primary metal-O_2 batteries [9]. Since primary metal-O_2 batteries exploit atmospheric oxygen as the cathode and eliminate traditional intercalation ion-based approach, they acquire comparatively higher theoretical specific energy density. Although the electric vehicle applications of Li-O_2 cells were not seen plausible by the authors at the time, the systems achieved high theoretical gravimetric energy density (11148 Wh kg^{-1} based on Li_2O_2 discharge product) which was close to that of gasoline (13000 Wh kg^{-1}). The subject was revived in 1990's by Abraham and Jiang by introducing the first nonaqueous Li-O_2 battery which composed of lithium as the anode, a gel polymer electrolyte

and a carbonaceous cathode [10]. In the cathode side, oxygen diffuses through the permeable electrode and gets reduced during the discharge process in order to generate electric power, however, the systems lost the attention during next decade in order to technical difficulties of attaining high energy densities and cycle life. Later on 2006, a Li-O_2 cell was made by Bruce et al. in which the polymer electrolyte was replaced by an organic electrolyte and the deposited Li_2O_2 on cathode electrode during discharge was decomposed to Li and O_2 during the charging process [11]. After this study, a huge attention was drawn to these cells around the world and a tremendous number of studies were dedicated to make these systems more feasible. Nevertheless, it was realized that the insulating nature of Li_2O_2 discharge product imposes high charging over-potential (typically > 1V) and low energy efficiency to the system and the limited natural resources of Li encouraged substituting this metal by the mostly abundant alkaline metal on the earth crust, i.e. Na. In 2013, Janek and Adelhelm introduced the first NaO_2 based Na-O_2 battery, in which comparatively lower charge overpotential ($<$ 0.2 V) was achieved due to the facilitated decomposition kinetics of superoxide species [12]. This behavior motivated much research on these systems and ever since there have been several investigations in order to get a better understanding of the working mechanism and improve the performance of the systems.
In this part, a brief explanation of the different terminologies used to describe batteries and their performance is presented. Anode- This electrode reverses during discharge and charge. Anode is the negative electrode during discharge and the positive electrode during charge and it reversibly dissolves inside the electrolyte and gives the load (electron) to the circuit.

Cathode- Like the anode electrode, the cathode electrode reverses and it is the positive electrode during charge and the negative electrode during discharge and it causes oxidation of the anode by taking the electron from it through the circuit.
Electrolyte- It is the chemical compound which provides electrically conducting solution by dissociating or fusing inside a polar solvent like water. When dissociated, it separates into cations and anions to conduct the electric current.
Battery Cell- It is composed of mainly three compartments including negative

and positive electrodes and electrolyte. The whole setup is made in order to store electrochemical energy.

Discharge- It is known as the conversion of the chemical energy of the battery into the electrical energy and withdrawing it to the load.

Charge- It is the conversion of the electrical energy coming from the external source into the chemical energy inside the battery.

Cycle- A complete sequence of discharge followed by charge or vice versa is called a cycle.

Battery Capacity- The total number of ampere-hours or watt-hours that can be withdrawn from the battery during discharge process before it reaches to the specified ending condition of discharge.

Current Rate- The amount of current which is applied to the battery during discharge or charge.

Cycle Life- The number of cycles under a specified condition that battery can perform before its capacity is considerably reduced. It is influenced by the depth of cycles (shallow or deep) and the cutoff of the charge.

Energy Density- The ratio of the accessible energy from the battery to its weight or volume (watt-hours/kilogram or watt-hour/liter).

Overpotential- it is known as the difference between the thermodynamically determined potential of the half reduction reaction and the actual potential which is measured by the experiments. Since in reality, the required energy to perform a reaction is more than the theoretically calculated one, the term is directly correlated to the voltage efficiency of the cell. Therefore, all of the conditions including environmental effects, battery compartments and most of all, current density have their individual effects on over potential. Normally, the overpotential is reported by the current density in which the experiment is taken place.

1.3 Working Mechanism of Na-O_2 Battery

Different types of electrolytes can be used to make a metal-O_2 battery cell in order to make them compatible with different applications and according to the

electrolyte type, there are four main cell architectures: (a) aprotic, (b) all-solid-state, (c) aqueous and (d) hybrid, as shown in Figure 1.2 [13]. The cathode active material is oxygen which should be supplied from the air or any other reservoir and metallic Na is the anode material for all types of the cells at the current stage. As can be seen in Figure 1.2 (b) and (c), a protective layer is required to make a hybrid or aqueous system in order to prevent the vigorous reaction between water and highly active Na metal. According to the many researches performed, the theoretical capacity of a non-aqueous system is higher than an aqueous system, since the chemical/electrochemical processes in aqueous systems include the reaction of O_2 with water and consequently dropping the cell capacity. There are very few studies about all-solid-state metal-O_2 systems since the metal conductivity of the solid state electrolytes is a limiting factor for these systems [14]. Since the non-aqueous Na-O_2 batteries are the most investigated systems among the others, we focus on non-aqueous Na-O_2 batteries in this thesis.

The performance of Na-O_2 batteries is dependent on many parameters including the type of cathode material and the non-aqueous electrolyte, humidity, O_2 pressure and CO_2 content [15, 16]. Among all parameters, cathode materials and non-aqueous electrolytes have attracted most of the research attention in Na-O_2 batteries in the early step of their development. Today, pure metallic Na is the most used anode material but regarding its highly active nature and safety

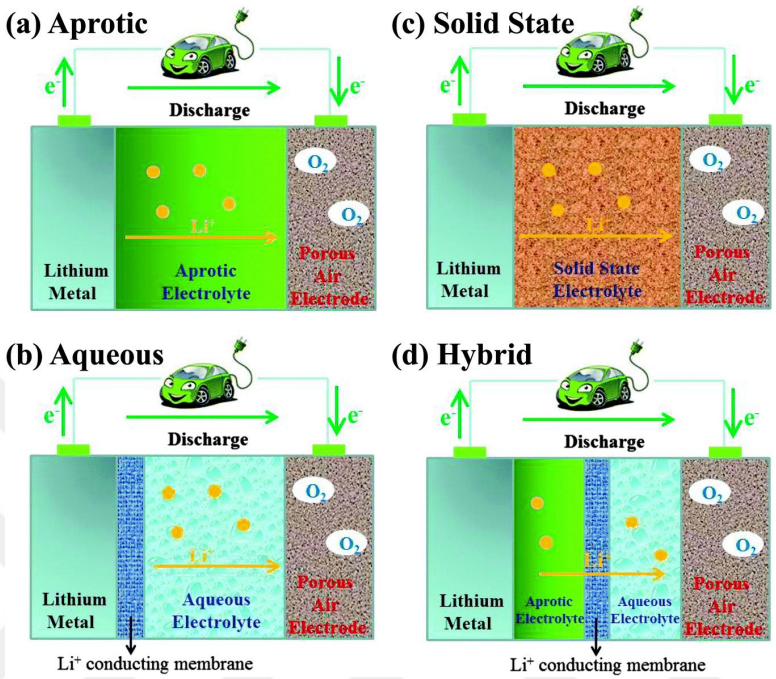

Figure 1.2: Schematic of the four different architectures of metal-O_2 batteries. (a) aprotic, (b) aqueous, (c) solid state and (d) hybrid [13].

issues, it should be replaced by some appropriate alternatives for future large scale production. However, the main issue today is to find a suitable cathode material which can catalyze the both ORR and OER reactions during discharge and charge processes, respectively [17]. The working principle of the non-aqueous Na-O_2 battery is schematically shown in Figure 1.3 [18]

Generally, the type of discharge product which is deposited on the cathode side during ORR has the main influence on the cell behavior during discharge/charge. To date, two main types of discharge products are reported in Na-O_2 battery studies including sodium superoxide (NaO_2) and sodium peroxide (Na_2O_2), therefore it is noteworthy to have a better understanding on how the thermodynamics and kinetics predict the formation of these products.

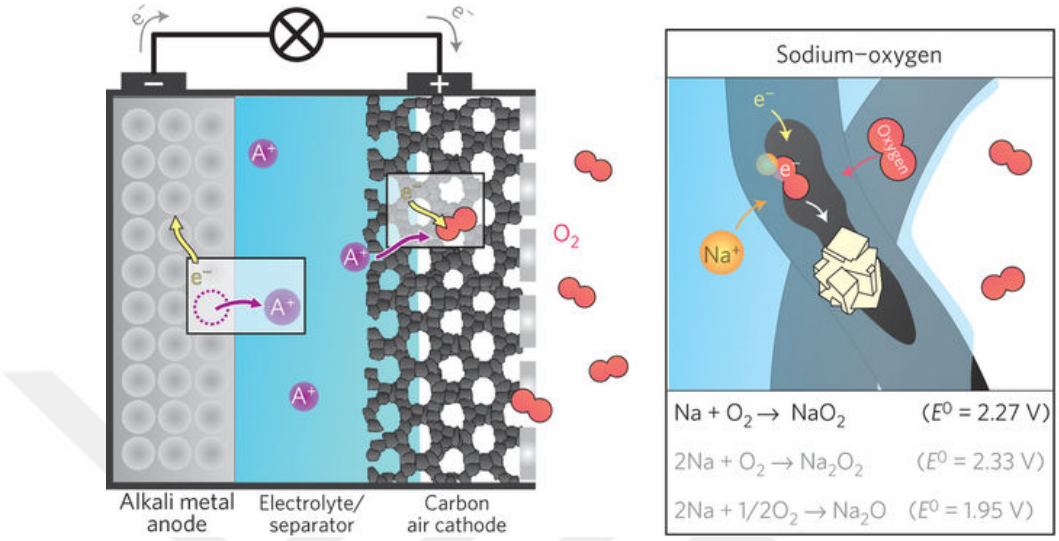

Figure 1.3: Working mechanism of a rechargeable Na-O_2 battery [19].

Equations (1.1)-(1-7) show the all possible reactions between Na and O_2 during discharge process in non-aqueous Na-O_2 batteries [12].

$Na^+ + e^- \rightleftharpoons Na\, E^0 = -2.71\,\text{vs}\cdot\,\text{SHE}$ (1.1)

$2\,Na^+ + 2\,e^- + O_2 \rightleftharpoons Na_2O_2\, E^0 = -0.38\,\text{V vs}\cdot\,\text{SHE}$ (1.2)

$2\,Na + O_2 \rightleftharpoons Na_2O_2\, E^0_{Na2O2} = 2.33\,\text{V vs}\cdot\,Na/Na^+$ (overall reaction) (1.3)

$Na^+ + e^- + O_2 \rightleftharpoons NaO_2\, E^0 = -0.44\,\text{V vs}\cdot\,\text{SHE}$ (1.4)

$Na + O_2 \rightleftharpoons NaO_2\, E^0_{NaO2} = 2.27\,\text{vs}\cdot\,Na/Na^+$ (overall reaction) (1.5)

$2\,Na^+ + 2\,e^- + \frac{1}{2}\,O_2 \rightleftharpoons Na_2O\, E^0 = -0.76\,\text{V vs}\cdot\,\text{SHE}$ (1.6)

$2\,Na + \frac{1}{2}\,O_2 \rightleftharpoons Na_2O\, E^0_{Na2O} = 1.95\,\text{V vs}\cdot\,Na/Na^+$ (overall reaction) (1.7)

Neither thermodynamics nor kinetics predicts the formation of Na_2O during discharge since it follows a two electron transfer reaction taking place at lower potential compared to NaO_2 and Na_2O_2. Although Na_2O_2 is thermodynamically more stable compared to NaO_2 ($E^0{}_{Na2O2} > E^0{}_{NaO2}$), the formation of NaO_2 is kinetically favored ($1e^-/O_2$) compared to Na_2O_2 ($2e^-/O_2$). Therefore, one can expect to have both of these products at the end of discharge. However, it seems that the cell architecture, cathode type, composition of the gas and humidity play the major roles to determine the discharge product type [20, 21]. The reaction can be written more specifically based on the formation and decomposition of peroxide or

superoxide during discharge/charge as following:

$O_2 + e^- \rightleftharpoons {O_2}^-$ (1-8)

$Na^+ + {O_2}^- \rightleftharpoons NaO_2$ (1-9)

$2\,{O_2}^- \rightleftharpoons O_2 + {O_2}^{2-}$ (disproportionation) (1-10)

$2\,Na^+ + {O_2}^{2-} \rightleftharpoons Na_2O_2$ (1-11)

In fact, the discharge product growth mechanism in Na-O_2 batteries is not straightforward and several groups tried to correlate discharge product formation to the mechanism underlying Li-O_2 batteries, due to the similarities of these two systems [22]. Since NaO_2 possesses a more pronounced contribution as the discharge product in Na-O_2 cells in recent years, a detailed information on NaO_2 formation/decomposition mechanism during battery cycling will be presented in the following section. Anyhow, more in-situ characterization techniques are required to deeply understand the mechanism underlying Na-O_2 batteries.

1.4 Critical Issues

considering that Na-O_2 batteries are introduced for less than a decade and the whole researches in this field are dedicated to get the basic knowledge about their mechanism and comparing these systems with state of the art Li-ion batteries and fuel cells, Na-O_2 batteries are in their infancy state, therefore, we need to address many parameters in order to achieve practical applications. The vague chemical and electrochemical reactions on the cathode side, improving the cell behavior by exploiting catalysts and stability of the battery compartments in the cell environment are the main critical challenges which are investigated in recent studies. In this section, we will discuss these three challenges in three parts.

1.4.1 Cathode Electrode Reactions

As mentioned in the previous section, discharge product formation mechanism in Na-O_2 batteries is quite reminiscent of that in Li-O_2 batteries. In both cases, there are two main routes for the formation of discharge products: solution mediated

and surface mediated routes [23]. However, it has been shown that both of the mechanisms play equivalently for the formation of NaO_2 in Na-O_2 batteries. As shown in Figure 1.4, in solution mediated route (route 1), oxygen gets reduced on the surface of the bare electrode and migrates to the already nucleated product in order to react with Na^+ and produce NaO_2. On the contrary, all of the processes including oxygen reduction and its reaction with Na^+ to deposit as NaO_2 takes place on top of already deposited NaO_2 in surface mediated route (route 2).

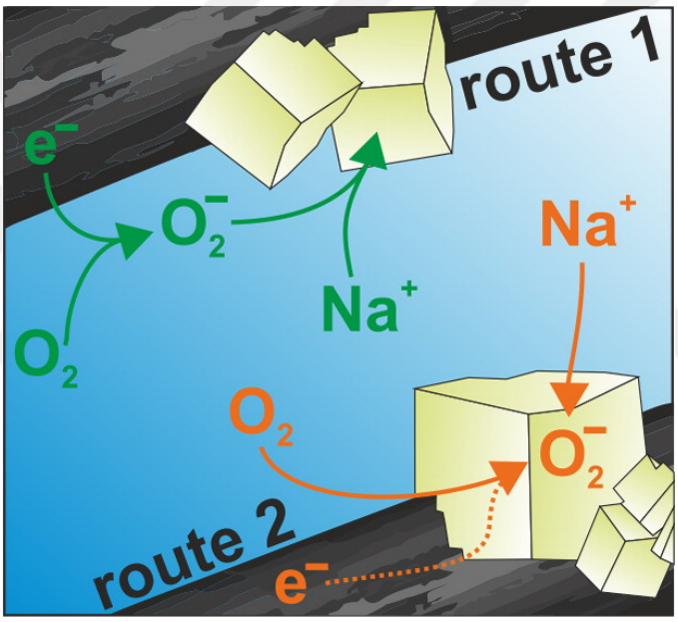

Figure 1.4: Schematic illustration of solution mediated route (route 1) and surface mediated route (route 2) for NaO_2 deposition during Na-O_2 battery discharge [23].

According to Nichols et. al., the surface mediated route is constrained by the insulating nature of NaO_2, therefore in the following steps of discharge, the solution mediated route is dominating [24]. However, due to the higher intrinsic conductivity of superoxide species than peroxide species, the solution mediated mechanism is expected to be more pronounced when NaO_2 is the main discharge product. The properties of deposited discharge product including its morphology and chemical composition are the factors affecting the electrochemical profile of

the system. Sayed et al reported that smaller NaO_2 particles can be deposited during discharge at high current densities compared to that of lower current densities [25]. On the other hand, according to Nichols et al, a film like NaO_2 is the dominating morphology in Na-O_2 batteries discharged at higher current densities, compared to that of cubic particles at lower currents [24]. However, according to Kim et al. NaO_2 is unstable in the cell environment and it dissolves inside the electrolyte by releasing highly active O_2^-, which consequently results in the formation of side products, specially $Na_2O_2.2H_2O$, through the following reactions [19]:

Discharge/charge: $Na^+ + O_2 + e^- \rightleftharpoons NaO_2$ (1-12)

dissolution: $NaO_2 \longrightarrow Na^+ + O_2^-$ (1-13)

Proton abstraction: $HA + O_2^- \longrightarrow HO_2 + A^-$ (1-14)

Disproportionation: $2\,HO_2 \longrightarrow H_2O_2 + O_2$ (1-15)

Oxidative decomposition: $A^- + HO_2 \longrightarrow CO_2, H_2O, OH^-$ (1-16)

Peroxo-hydroxylation: $2\,Na^+ + 2\,OH^- + H_2O_2 \longrightarrow Na_2O_2 \cdot 2\,H_2O$ (1-17)

Since the decomposition potential of resulting $Na_2O_2.2H_2O$ during charge is higher than the original NaO_2 discharge product, this process results in an unwanted charging over potential increase. Liu et al. and Reeve et al. reported that the highly active nature of NaO_2 not only causes decomposition of the electrolyte, it also attacks the carbonaceous cathode and its additives to form more detrimental side products including Na_2CO_3, NaF, Na_2O_2, etc [26, 27]. In this regard, a general trend was governed by a series of works investigating the effect of NaO_2 ionization on the cell electrochemistry: increasing the exposure time of NaO_2 to the electrolyte results in the elevated side products formation and consequently precipitous increase in charging over potential [19, 25, 28]. Therefore, the cell operating condition including the time interval between charge and discharge, charge and discharge current densities, the amount of water inside the electrolyte and etc. severely affect the properties of NaO_2 and the behavior of battery.

1.4.2 Battery Components Stability

During the last years, numerous studies have been carried out in the development of using organic electrolytes in Li-ion batteries, but there are several concerns in order to use them in Na-O_2 or Li-O_2 batteries. Followings are the ideal characteristics of an aprotic electrolyte to be exploited in Na-O_2 batteries. The most important issue of the aprotic electrolytes is their stability towards highly active reduced species (O_2^- and O_2^{2-}) and anode material as well as the decent solubility of O_2 inside it to enhance the mass transport to the cathode. The volatility of electrolyte is not desired in the cell environment due to concentration change, and lastly, a sufficient conductivity to maintain the high rate capability is desired. It is noteworthy that the stability of electrolyte is highly dependent on the stability of solvents, sodium anode and salts as well as the other additives.

Among the organic electrolytes, carbonate based electrolytes like propylene carbonate (PC), dimethyl carbonate (DMC) and ethylene carbonate (EC) have been widely used in the early stage of the development of Li-O_2 and Na-O_2 batteries [11]. However, it was realized that decomposition of these electrolytes severely occurs in the presence of O2 during discharge process and the formation of poisonous side products is non-negligible. Na_2CO_3 and Li_2CO_3 are the main side products which accumulate on the electrode surface and their decomposition potential during charge is higher than the main discharge products. On the other hand, LiOH and NaOH are the other decomposition side product by the reaction of moisture contaminant and the metallic anode or discharge products. As a result, the over potential increment during charge is inevitable. Therefore, many researches have been focused on finding proper electrolytes to replace in these cells.

Ether based electrolytes are the suitable candidates in order to substitute carbonate based electrolytes in Na-O_2 and Li-O_2 batteries, regarding their numerous advantages including higher stability towards discharge products and O_2 reduced species, higher decomposition potential ($>$ 4 V vs. Li/Li^+), low volatility, decent wetting property, safety and cheaper price. The most famous ether based

electrolytes are tetraethylene glycol dimethyl ether (TEGDME or 4G) and 1,2-dimethoxyethane (DME). Although Li_2O_2 and NaO_2 are the main discharge products in ether based batteries, it is shown that different side products are identified alongside the main products [29–32]. Therefore, the lower round-trip efficiency, cycling stability and poor rechargeability can be induced by side products. However, ether based electrolytes are the mostly used electrolytes in these systems currently, despite the formation of side products.

Na salt is the other main compartment of the electrolyte and its characteristic has a big influence on determining the reversibility and capacity of Na-O_2 systems. Although Na salt should possess a decent solubility in the solvent to supply Na^+ to the system, its anion should be also stable in the cell environment in contact with the battery compartments (separators, Na anode, ...), solvents and the reduced O_2 species. According to Lutz et al., although the type of anion does not affect NaO_2 deposition and the capacity, it severely changes solid electrolyte interface (SEI) stability on the anode side and by decreasing the donor number of the anion, a more stable SEI layer can be formed. In this regard, ClO_4^- had the most stable SEI layer and on the contrary, by using $TFSi^-$, the degradation occurred in SEI layer [33].

Using a metallic Na anode is another concern in the application of Na-O_2 batteries due to Na dendrite formation and safety issues, which constrains its commercial applications. However, since the stability of aprotic electrolyte and the cathode are the biggest issues in these systems which the recent studies have been struggling with, pure metallic Na is still being used as the anode electrode. Anyhow, during discharge/charge cycles with higher cycle numbers or deeper cut off capacity, Na dendrite formation is a severe problem [34]. Dendrites in commercial Li-ion batteries can penetrate through the separators and cause the short circuit inside the battery, which results in overheating of the cell and catching fire. As mentioned, the formation of a stable SEI layer is another issue for anode side which should be taken into account by choosing appropriate salts and electrolytes.

1.5 Cathode Materials for Na-O_2 Battery

Although Na-O_2 batteries benefit from the low cell over potential compared to Li-O_2 batteries due to the facilitated ORR/OER kinetics of superoxide species, as mentioned in the previous sections, severe time dependent side products formation causes precipitous over potential increase during charge in these systems. Even if carbonaceous materials have been reported as a suitable cathode material for Li-O_2 and Na-O_2 batteries, they are unable to effectively facilitate OER reaction. On the other hand, the intrinsically lower capacity of Na-O_2 batteries compared with Li-O_2 batteries requires choosing a proper type of electro catalysts to maximize the capacitance in these systems. Therefore, the new category of cathode materials is required for these purposes.
Various types of catalyst materials have been investigated for the application of fuel cells and other metal-O_2 batteries in order to minimize the ORR/OER over potentials. The catalyst should be designed to be optimized in the case of structure, morphology and phase to effectively increase the energy efficiency of the battery. In the following section, a detailed information about the selection criteria of a proper catalyst material has been presented.

Among all of the characteristics for better batteries, there are four major factors which have the main role in determining the battery performance: specific capacity, round trip efficiency, cycling performance and rate capability, which all can be effectively improved by employing electrocatalysts in the battery [35]. As mentioned above, detrimental side products formation is one of the main reasons for increasing over potential in Na-O_2 batteries. Also, the precipitated discharge products can block the O_2 diffusion pores and cause the discharge termination and limited specific capacity [36]. Therefore, the material design to optimize sufficient pore distribution of the cathode and also satisfactory electrode-electrolyte interaction in order to supply ionic transfer are crucial parameters [37–39]. On the other hand, the cathode material should be able to catalyze ORR/OER effectively. Recently, many catalyst materials which have performed as the electrode in fuel cells and other metal-O_2 batteries have been investigated for Na-O_2 and

Li-O_2 batteries and in this section, we will mention about carbonaceous materials and transition metal oxides, which are the cathode materials employed in this study.

1.5.1 Carbon Materials

Among all types of materials employed in energy storage applications, carbon materials are the most common ones due to their superior properties including high surface area and electrical conductivity, low price, light weight and corrosion resistivity [40, 41]. Besides, they are easy to prepare as different cathode forms and shapes and possess acceptable ORR/OER catalytic activity [42].
Due to aforementioned reasons, carbon materials are widely used as catalyst for Li-O_2 and Na-O_2 applications. Commercial carbon materials like Vulcan XC72, Ketjen Black and Super P have been used in Na-O_2 and Li-O_2 systems [26, 43–45]. For the commercial carbon materials, defect density and pore size distribution are the important factors specifying the performance of these types of products, specially their specific capacity [46]. Recently, commercial carbon fibers are also exploited in Na-O_2 batteries due to their unique structure [47]. Although these materials present decent capacity when they are used in suitable electrolyte and combined with additives, still better materials are required in order to obtain capacities near to theoretical capacities of Na-O_2 batteries.
Carbon nanotubes (CNTs) are very promising candidates as alternative for commercial carbon materials. Extremely high surface area and electron conductivity, mechanical strength, thermal and chemical stability and high elasticity make this material a suitable choice as cathode material for Na-O_2 systems. Numerous researches in Li-O_2 and Na-O_2 fields have been reported decent catalytic activity and ease of handle and characterization of this material [32, 48–51]. Therefore, it has been chosen as the support material in this study.

1.5.2 Catalysts

Transition metal oxides (TMOs) are the most used catalysts for Li-O_2 and Na-O_2 applications due to their high activity to facilitate ORR/OER. Manganese oxide, cobalt oxide, iron oxide, palladium oxide and molybdenum oxide are among TMOs which are mostly reported for Li-O_2 and Na-O_2 applications, especially by Bruce and co-authors [11, 52–55].

Cobalt oxide is one of the commonly used catalysts for Li-O_2 and Na-O_2 applications. In Li-O_2 case, it has been reported that this material can achieve a low charging over potential and a decent capacity retention. Riaz et al. concluded that the morphology/architecture of cobalt oxide has a major effect on its catalytic performance by preparing different morphologies of this material including nano sheets and nano needles [56]. Wen et al. reported the discharge product morphology control by using Co_3O_4 in Na-O_2 batteries and consequently improved cycling performance of the cell [57]. Sun et al. prepared CNT@Co_3O_4 by atomic layer deposition of cobalt oxide on CNTs [58]. It was shown that a composition of NaO2/Na2O2 (NaO_x) can be achieved by using CNT@Co_3O_4 and it can provide the electrochemical decomposition of sodium superoxide, sodium peroxide and sodium carbonate at lower over potentials compared to bare CNT. Manganese based oxides (MnO_x) are another types of TMOs which are actively explored in Na-O_2 and Li-O_2 applications which can increase round-trip efficiency and specific capacity. Yadegari et al. revealed ORR/OER mechanism in Na- and Li-O_2 batteries by using a solid state Pd-Mn_3O_4 catalyst [59]. They proved that ORR/OER catalytic reactions in these systems originate from the stabilization of O_2^- intermediate species on the surface of the catalyst. They correlated the catalytic activity of TMOs to the bonding energy of O_2 species to these materials, in which the higher bonding energy of O_2 to the catalyst surface results in better catalytic performance.

Recently, ruthenium oxide has taken great attention as the catalyst material for Li-O_2 and Na-O_2 batteries applications, especially due to its excellent catalytic performance for OER. Yilmaz et al. prepared a RuO_2 NP coated CNT as a catalyst in Li-O_2 batteries [49]. Although by using RuO_2 NP the specific capacitance of the cell was not affected, the electrical efficiency of the battery was improved

73%. According to their results, a film like amorphous Li_2O_2 is deposited by using RuO_2 NP during ORR, which its high electrolyte/electrode interface and non-crystalline nature result in its decomposition at lower over potential during OER compared to crystalline toroidal Li_2O_2 particles. Micrometer sized RuO_2/boron doped graphene was used as a catalyst in Na-O_2 batteries by Wu et al. [60] It was shown that by using RuO_2, the composition and structure of original discharge product (NaO_2) severely changes and an amorphous $Na_{2-x}O_2$ can be deposited in cathode during ORR. Similarly, the amorphous discharge products can decompose at potentials lower than that of crystalline particles, which is due to the more thermodynamic stability of crystalline phases. Therefore, regarding RuO_2 applicability in different systems and its ease of synthesis, as well as its non-identified behavior in Na-O_2 batteries, it has been chosen in this study as the TMO catalyst for Na-O_2 applications.

Shortly, TMOs possess several pros in order to be used for ORR/OER applications in Na-O_2 batteries such as their high activity of catalytic ORR/OER reactions, ease of preparation in different phases and morphologies, their compatibility with different support materials including carbon materials, low price, stability at high potentials and environmentally friendliness. However, the main disadvantage is their heavy nature and high price (like RuO_2), which urges scientists to make composite materials containing TMOs on different substrates. In this regard, both catalytic activity and electrical conductivity can be increased due to the synergistic effect of TMOs and the substrate material. However, new catalyst composites preparation methods are required in order to make them feasible for scaling up and commercial applications.

1.6 Motivation

Various materials have been used as cathode material for Na-O_2 applications, but the exact mechanisms underlying catalytic reactions have not been reported yet, especially in the case of NaO_2 as the main discharge product. As mentioned in the previous section, there are couple of detailed reports of catalysts for Na-O_2

applications but in those researches, the nature of NaO_2 discharge product undergoes a composition evolution by using catalyst, therefore, the catalyst effect on the physical properties of NaO_2 and its consequent effect on the cell electrochemistry is not realized yet. Due to NaO_2 instability in the cell environment and its dissolution in the electrolyte during storing span, the effect of catalyst on this behavior is also expected to be motivating.

Since the electrochemical and chemical processes underlying Na-O_2 batteries are pretty complicated, especially with NaO_2 as the main discharge product, a very well known catalyst should be chosen to make sure about its ORR/OER activity, in order to minimize the complication of the investigating parameters. RuO_2 is the best candidate in this regard since there are numerous researches about its excellent performance in different media (aqueous and non-aqueous) and systems (fuel cells and metal-O_2 batteries). Also, this material can be easily synthesized in different phases and morphologies. Therefore, it is a suitable catalyst candidate for this study.

In order to minimize agglomeration effect of prepared RuO_2 NP, increase its electrical conductivity and stability, a backbone material is required. Today, CNT is one the most used support material for composite preparation in the catalysis field due to its aforementioned properties. So, it has been chosen as the substrate for RuO_2 NP deposition by a microwave assisted hydrothermal method.

In the second part of this thesis, a 3-D structure of bi-functional RuO2/Mn2O3/carbon nanofiber (CNF) catalyst has been synthesized and used as a cathode for Na-O2 batteries. In this part, we tried to eliminate the intrinsic low specific capacity of Na-O2 batteries by incorporating Mn2O3 nanorods decorated with RuO2 NPs, as a strategy to increase activity and exposed surface area for ORR/OER. Our results in this part indicate that RuO2/Mn2O3/CNF shows a better battery performance (capacity and overpotntial) compared Several characterization techniques including scanning and transmission electron microscopy, Raman spectroscopy, X-ray diffraction, nuclear magnetic resonance, X-ray photoelectron spectroscopy and electrochemical investigations are employed in this study to confirm the proposed RuO_2 catalytic mechanism in Na-O_2 batteries.

Chapter 2

EXPERIMENTAL

2.1 RuO_2/CNT and CNT Cathodes Preparation

RuO_2/CNT composite was prepared through a facile microwave assisted hydrothermal synthesis method. 20 mg pristine CNT (>95% purity, diameter 20 nm, Sigma Aldrich) was dispersed in 20 ml DI water by using 30 min bath sonication. Then, 40 mg $RuCl_3.xH_2O$ (99.9%, Alfa Aesar) was dissolved in the solution by vigorous stirring for another 30 min. The resulting mixture was transferred to a vessel and microwave assisted hydrothermal reaction was performed at 180°C for 30 min in microwave synthesis reactor (Anton Paar Monowave 300). After the reaction was performed, resulting powder was washed and centrifuged with DI water and ethanol for at least 5 times and dried in an oven at 60°C for overnight. Finally, the resulting RuO_2/CNT powder was annealed at 150°C for 1 h in ambient atmosphere. For cathodes preparation, RuO_2/CNT was ground with pristine CNT with the mass ratio of 6:4 and dispersed in isopropanol by 15 min tip sonication and 0.3 mg of the powder was deposited on top of the pressed Ni-foam (∼12 mm diameter) for battery measurements. The free standing and binder free film cathodes were prepared by vacuum filtration of the resulting slurries. After

drying at 60°C, the films were peeled off from the glassy fiber C (GF/C, Whatman) and dried under vacuum at 70°C for overnight prior to use. CNT cathodes and free standing films were also prepared by the same procedures. The diameter and mass of the resulting films were 12 mm and ∼3.6-3.8 mg, respectively.

2.2 Fabrication of CNF

A mixture of PAN (Polyacrylonitrile, MW ∼150,000 g/mol^{-1}, Scientific Polymers) and PMMA (poly(methyl methacrylate, MW ∼350,000 g/mol^{-1}, Sigma Aldrich) solution (10 wt% in DMF (N,N-dimethylformide, ACS reagent, ≥ 99.8%, Sigma Aldrich) PAN:PMMA weight ratio of 95:5) was prepared by mechanically stirring for overnight to obtain homogeneous polymer solution for the electrospinning of nanofibers. Electrospinning of the solutions was carried out at 15 kV and 16 cm distance between the collector and the tip of the syringe. Carbon nanofibers (CNF) were prepared with a two-step heat-treatment of electrospun polymeric nanofibers in a high temperature furnace. The oxidative stabilization was carried out at 280°C for 2 h with heating rate of 5°C/min under air atmosphere and the carbonization was done at 800°C under argon atmosphere for 2 h with a heating rate of 5°C /min.

2.3 Preparation of Mn_2O_3/CNF, RuO_2/CNF and RuO_2/Mn_2O_3/CNF

In the first step, Mn_2O_3/CNF (MC) composites were prepared by a facile microwave synthesis method. Typically, 20 mg of electrospun CNF (fabrication details in supplementary information) was dispersed in 20 ml DI water by 10 min sonication. Then, different amounts of $KMnO_4$ were mixed with the CNF dispersion and stirred in the room temperature for 30 min. The above dispersions were added to the vessels and the microwave-assisted hydrothermal reactions were

performed at 180°C for 30 min in the microwave synthesis reactor (Anton Paar Monowave 300). The amount of $KMnO_4$ was adjusted to 0.25 mmol to result MC sample. After the reaction was performed, MC sample was washed and centrifuged with DI water and ethanol for several times and dried in an oven at 60°C for overnight. Finally, the sample was annealed for 1 h in 150°C in the air atmosphere.

For RMC preparation, 20 mg MC was dispersed in 20 ml DI water by 5 min sonication and 0.025 mmol of $RuCl_3.xH_2O$ was mixed with the solution by stirring for 30 min. Then, the resulting mixture was added into the vessels and put in the microwave synthesis reactor at 180°C for 20 min to result RCM sample. Figure 2.1 shows the schematic illustration of RMC sample preparation sequence. During the whole microwave synthesis preparation of MC and RMC, the mixers were stirred at 600 rpm. After the reaction was complete, the product was washed,

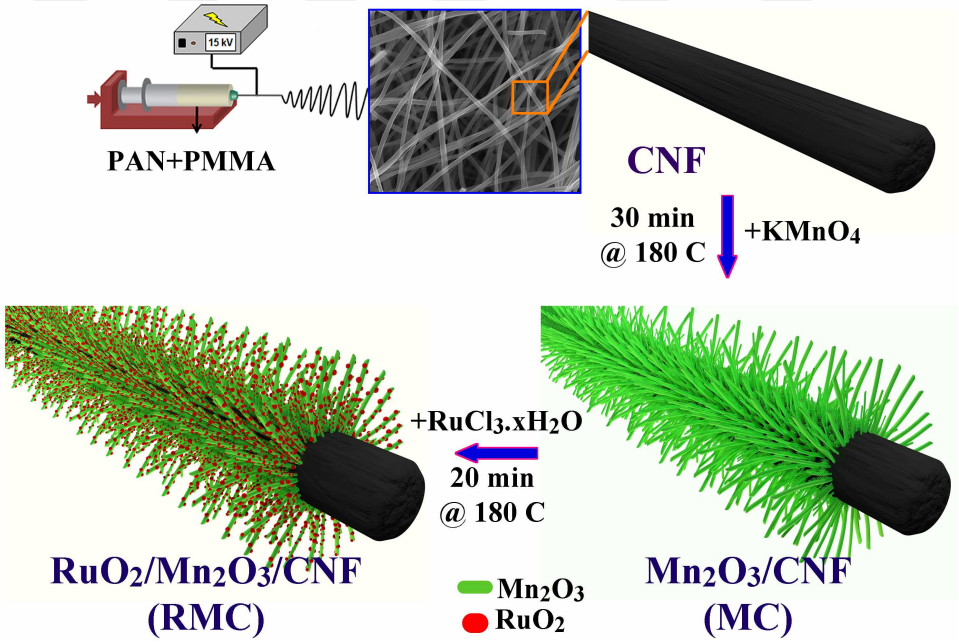

Figure 2.1: Schematic illustration of 3D RMC composite preparation. Electrospun-CNF was used as the backbone for Mn_2O_3 nanorods deposition in the first hydrothermal step. Then, RMC was prepared during the second hydrothermal step by using MC as the template for RuO_2 nano-particles deposition.

dried and annealed same as MC sample.

For the preparation of RC, the same procedure as RMC was applied, but MC was replaced by CNF as the substrate for RuO_2 deposition.

The cathodes were prepared by drop-casting the active materials (20 wt.% C65 containing CNF, MC, RC and RMC) on both sides of Ni-foams ($\sim$12 mm diameter). The mass of active materials on cathodes was $\sim$0.5 mg.

2.4 Na-O_2 Cell Assembly

All the procedures during cell assemblies were carried out in an Ar filled glove box (O_2 level <0.5 ppm, H_2O level <0.5 ppm). The cathodes and Na-O_2 cell components were dried at 70°C in a vacuum oven for the overnight before cell assemblies. The Na-O_2 cells were composed of metallic Na (ACS Reagent, Sigma Aldrich) covered stainless steel plate as the anode electrode, Celgard 2500 and GF/C as the separator, RuO_2/CNT or CNT as the cathode electrodes and 280 μ of the electrolyte. The electrolyte was prepared with tetraethylene glycol dimethyl ether (>99%, Sigma Aldrich) which contained 0.5 M $NaCF_3SO_3$ (NaOTf, 98%, Sigma Aldrich). The salt was purified according to the procedure reported by McCloskey et al. [22] and the solvent was dried using 3 Åmolecular sieves for over 7 days. The water amount of the final electrolyte was <10 ppm according to Karl Fischer titration.

2.5 Electrochemical Characterizations

Electrochemical examinations of the Na-O_2 cells were conducted using a battery cycler (Landt Instruments, CT2001A) after at least 8 h relaxation under Ar atmosphere and 3 h relaxation under 1.5 atm of O_2 pressure (40 ml of volume capacity integrated O_2 tank). The specific capacities and current densities were calculated according to the total mass of active materials on the cathodes.

2.6 Further Characterization Methods

Discharged or charged cathodes were extracted from disassembled Na-O_2 cells inside Ar filled glove box and washed with at least 3 ml acetonitrile (anhydrous, >99.9%, Sigma Aldrich) in order to remove residual electrolyte and dried under the vacuum without exposure to air. Morphological and structural characterizations were performed by scanning electron microscope (SEM, FEI-Quanta 200 FEG) operating at 5 kV and transmission electron microscope (TEM, FEI Tecnai G2 F30) operating at 100 kV. For the TEM sample preparation, fully discharged cathodes were scratched and resulting powders were applied on lacy carbon coated TEM copper grid. X-ray diffraction (XRD) patterns were collected using a Pananalytical instrument (X'pert Pro MPD, Cu-Kα radiation, λ= 1.5405 Å). The XRD patterns were collected over the 2θ range of 30°-50° using Kapton tape for isolating the samples from air exposure. High-resolution X-ray photoelectron spectroscopy (XPS, Thermoscientific, K-Alpha, Al K-α radiation) was performed on pristine and cycled cathodes and Raman spectra were collected on a confocal Raman instrument (WITec alpha300) by using an air tight sample holder. ^{1}HNMR spectroscopy was performed using a 400 MHz Bruker NMR system. The samples after discharge or partial/complete charge were immersed in 0.6 ml D_2O (Sigma Aldrich) under Ar atmosphere and the resulting solutions were collected for the measurements.

Chapter 3

RESULTS AND DISCUSSION

3.1 RuO_2/CNT Cathode

The RuO_2/CNT composite was synthesized through a one pot microwave-assisted hydrothermal reaction. TEM images of the prepared composite show the uniform distribution of RuO_2 NPs with an average diameter of 1.72 nm on CNT surface (Figure 3.1a). The C1s X-ray photoelectron spectroscopy (XPS) spectrum of RuO_2/CNT (Figure 3.2a and b) exhibited one pair of Ru^{3d} doublet for RuO_2, alongside C^{1s} peaks corresponding to CNT. The XPS Ru^{3d} spectrum exhibits three pairs of Ru^{3d} doublets including RuO_2 (∼281.8 eV), $RuO_2.xH_2O$ (∼282.7 eV) and the satellite feature (∼283.6 eV) along with C^{1s} species arising from CNT. The hydrated form of RuO_2 ($RuO_2.xH_2O$) seen in this study is due to the high affinity of RuO_2 to water which still remains under ultra high vacuum (UHV) [61, 62]. The O^{1s} spectra further confirms the presence of lattice oxygen (Ru-O at ∼530.7 eV), hydroxyl group along with satellite feature (∼532.7 eV) and the oxygen containing carbon bonds (∼533.7 eV) [62, 63]. The Raman spectrum of RuO_2/CNT consists of the well-known D-, G-, 2D- and D+G-bands of CNT and two peaks at 520 cm^{-1} and 631 cm^{-1} relating to the first order E_g and A_{1g} phonon bands of rutile RuO_2 (Figure 3.2c) [64]. According to XPS and Raman results, the prepared samples are mainly composed of RuO_2. Both CNT and

RuO_2/CNT electrodes presented same uniform pore size and distribution with entangled micron sized CNTs (Figure 3.3).

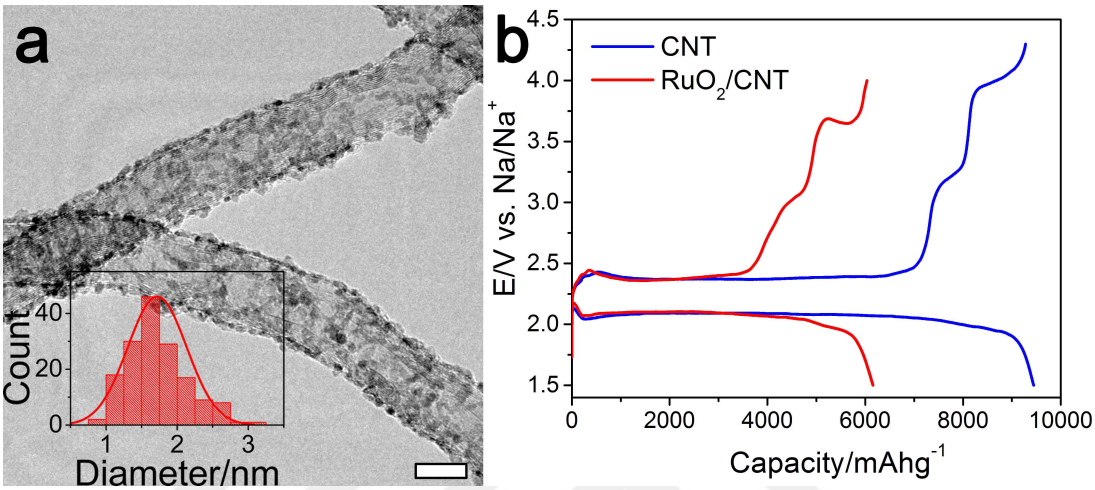

Figure 3.1: (a) TEM image of RuO_2/CNT and RuO_2 particle size distribution over CNTs (scale bar indicates 10 nm). (b) First DC/RC curves of CNT (blue) and RuO_2/CNT (red) at a current density of 100 mAg^{-1} and discharge cutoff potential of 1.5 V.

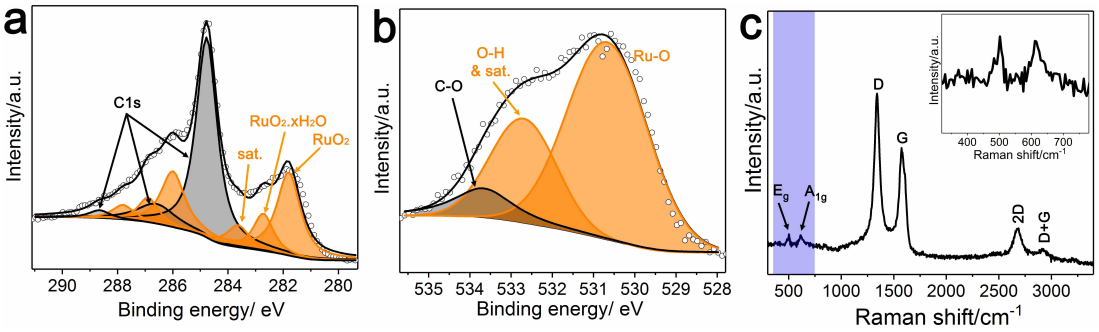

Figure 3.2: Characterization of RuO_2/CNT by XPS (a) Ru^{3d}, (b) O^{1s} and (c) Raman spectroscopy. The inset in (c) is the enlarged graph of the shaded spectrum.

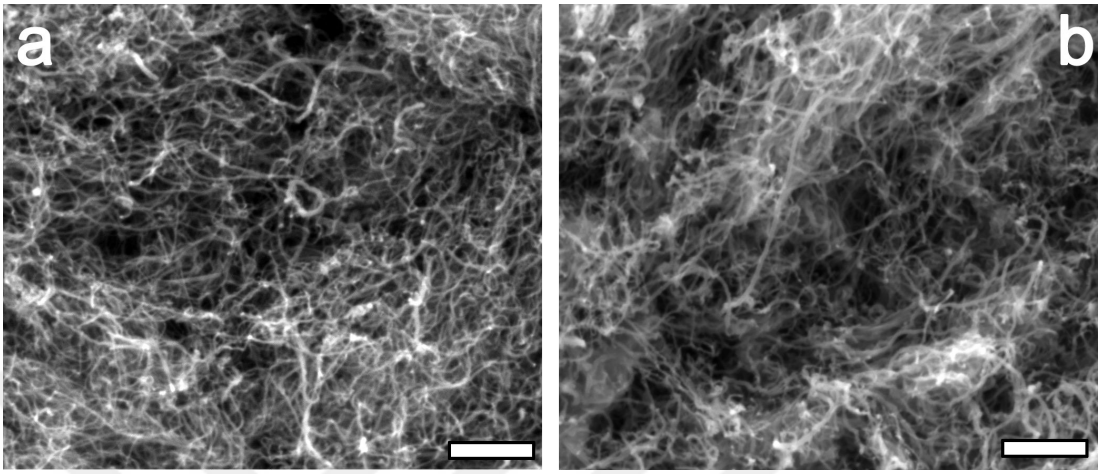

Figure 3.3: SEM images of pristine (a) CNT and (b) RuO_2/CNT. Both of the samples show same pore size and distribution. The scale bars represent 500 nm.

Binder free cathodes (CNT and RuO_2/CNT) drop-casted on Ni-foam were utilized in Na-O_2 cells. Galvanostatic discharge/recharge (DC/RC) measurement of the first cycles at 100 mAg^{-1} current density in Figure 3.1b shows that RuO_2/CNT delivered a lower specific capacity (6157 $mAhg^{-1}$) compared to CNT (9444 $mAhg^{-1}$) at the end of DC with the cutoff potential of 1.5 V. The film NaO_2 growth on RuO_2/CNT during DC and blocking the active surface sites may be the reason for RuO_2/CNT lower capacity (will be discussed in Figure 3.10). During RC, three distinct regions were observed for both cathodes: i) a plateau around 2.38 V, corresponding to NaO_2 decomposition [12], ii) a short slope between 3 and 3.3 V and iii) a plateau above 3.5 V, which regions (ii) and (iii) are corresponding to the decomposition of side products, mainly $Na_2O_2.2H_2O$, NaOH, carbonate and carboxylates [65, 66]. A detailed analysis of identifying the products responsible for each plateau is presented in Figures 3.4-3.8. For regions (ii) and (iii), respectively around 0.357 V and 0.336 V charging potential reductions were found in the RC curve of RuO_2/CNT compared with CNT, implying that RuO_2 actively contributes to the decomposition of side products during OER. A more detailed analysis of the effect of RuO_2 on DC and RC behavior of Na-O2 cell will be presented in the subsequent parts of this work. It is noteworthy that

region (iii) does not stand for electrolyte decomposition, as no plateau was observed under during RC of fresh cells (Figure 3.9) in which the extracted currents are believed to be due to the electrolyte decomposition.

A stepwise DC/RC cycle was performed in order to recognize the nature of products in each plateau, as shown in Figure 3.4. The C^{1s} spectra of the DC and RC 2.6 V samples show the coverage of the samples by carboxylate decomposition products (Figure 3.5). The dominance of the peaks at ∼286 and ∼290 eV for these samples is respectively indicative of -C-O-Na (formate, acetate) and C=O (sodium acetate/formate, sodium carbonate) abundance on the samples, as well as C-F group at ∼294 eV corresponding to the anion decomposition products [33, 67]. It is noteworthy that C-C signal at ∼284.8 is not apparent in DC samples and RuO_2/CNT RC 2.6 V sample, due to the cathode surface coverage by the products (Figure 3.7). According to C1s spectra it can be concluded that NaO_2 surface is highly active towards the electrolyte decomposition and most of the degradation products are decomposed after RC. After DC, XPS O^{1s} spectra of both samples (Figure 3.6) show a strong NaO_2 peak at ∼532 eV, together with a peak at ∼534 eV corresponding to C-O from carboxylate products, as observed in C^{1s} spectra. Once the samples are recharged to 2.6 V, the ratio of C-O:NaO_2 increases, indicating NaO_2 decomposition during the lowest potential plateau. After RC, NaO_2 completely diminishes, suggesting its complete decomposition after RC. The peak at ∼537 eV corresponds to the residual oxygen moieties on carbon [67]. According to SEM images of the stepwise samples (Figure 3.7), the surface of both electrodes is getting cleaner by continuing charge, and they recovered to the original morphology after complete RC. According to ^{1}HNMR results (Figure 3.8), ^{1}H chemical shifts (δ) of HDO, tetraglyme, acetate and formate are observed at 4.78, 3.35-4, 1.92 and 8.46 ppm [49], respectively, compatible with the XPS results.

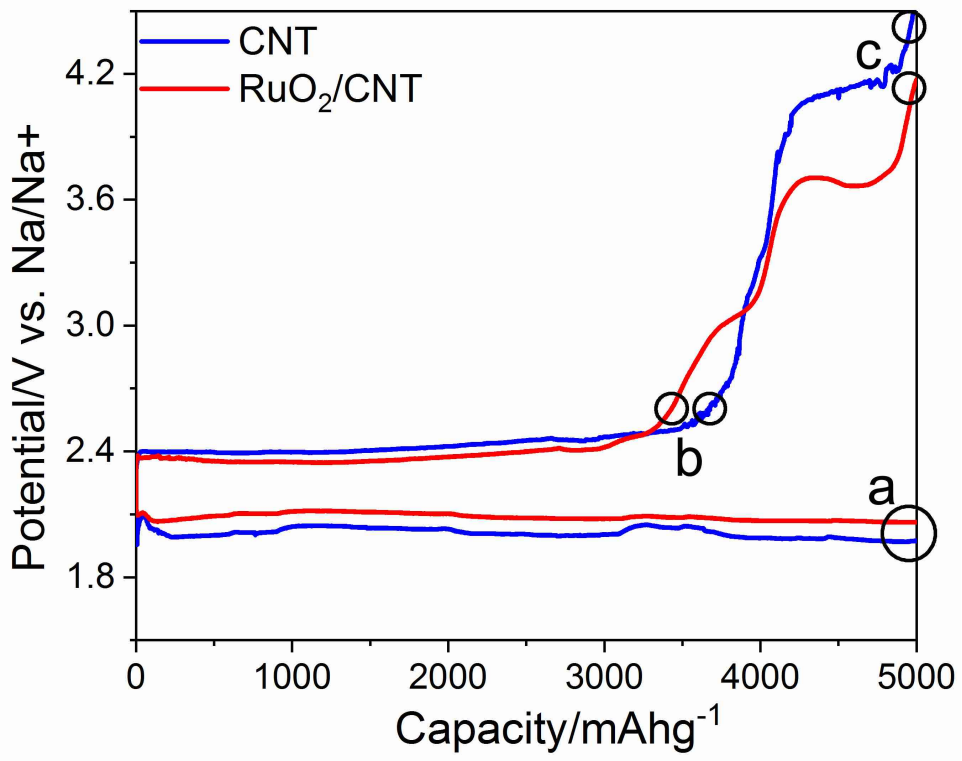

Figure 3.4: The stepwise DC/RC cycling of RuO_2/CNT and CNT with a limited capacity of 5000 $mAhg^{-1}$ at a current density of 100 mAg^{-1}. After each step (a: DC, b: RC to 2.6 V and c: RC), the cells were disassembled and the cathodes were rinsed with acetonitrile for post mortem characterizations by XPS, SEM and NMR (Figures 3.5-3.8) in order to recognize the identity of products responsible for each plateau.

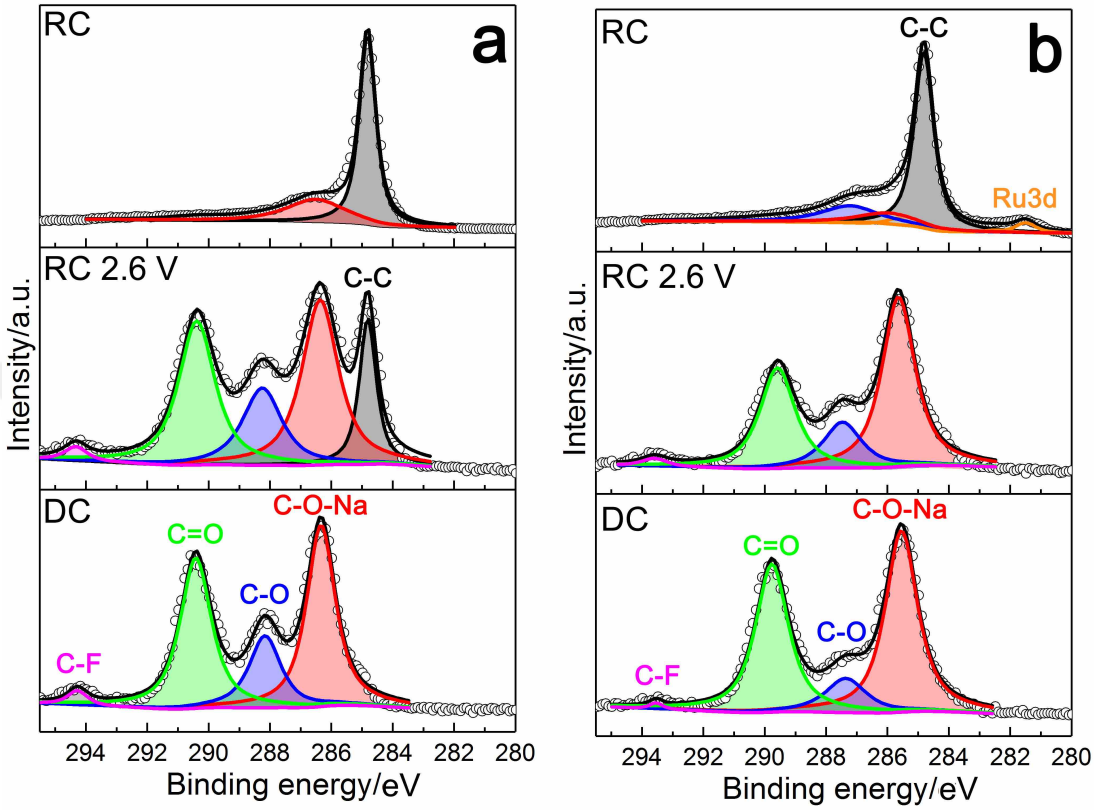

Figure 3.5: XPS C^{1s} spectra of the stepwise cycled (a) CNT and (b) RuO_2/CNT in Figure 3.4.

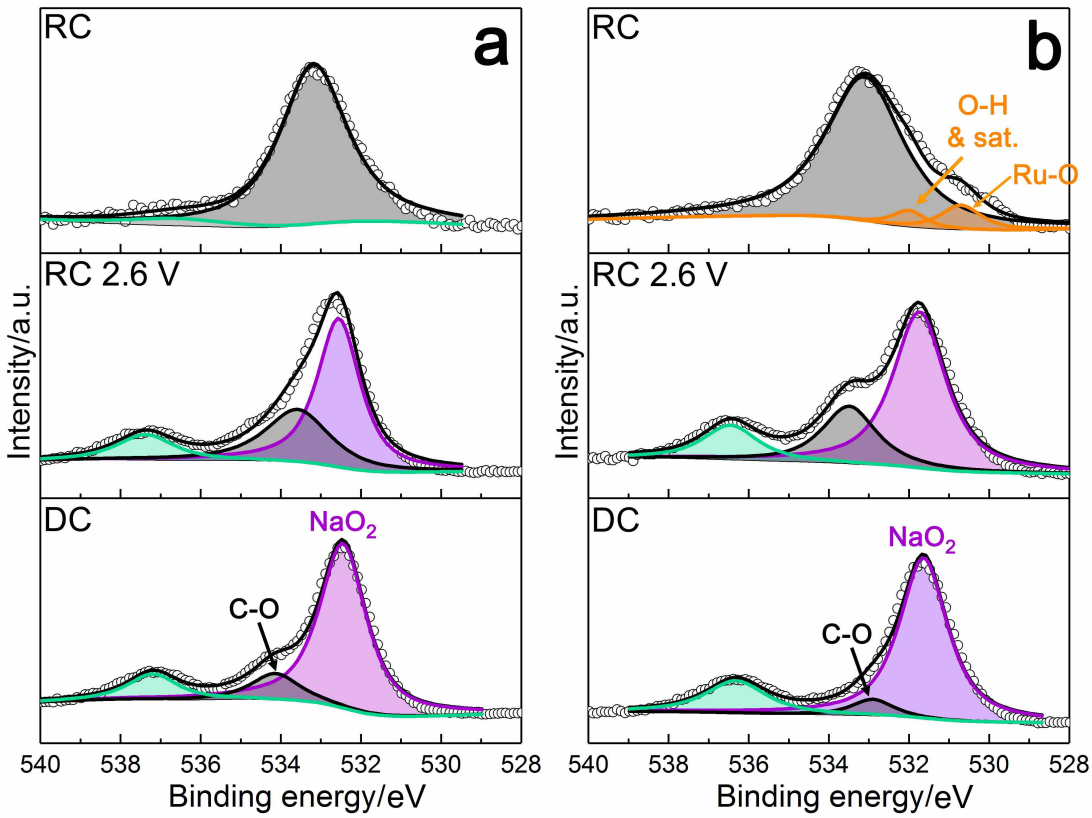

Figure 3.6: XPS O^{1s} spectra of the stepwise cycled (a) CNT and (b) RuO_2/CNT in Figure 3.4.

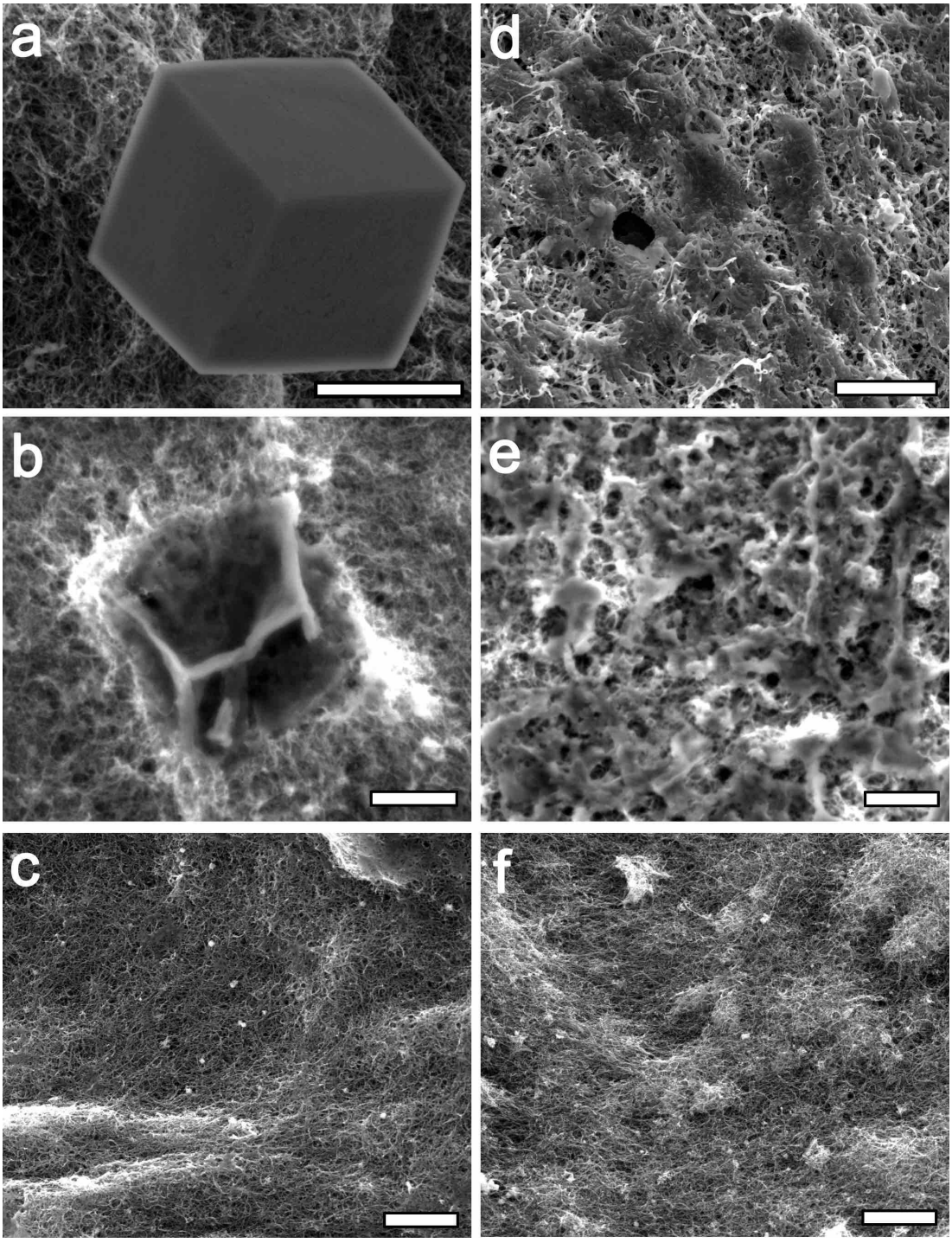

Figure 3.7: SEM images of the stepwise cycled (a-c) CNT and (d-f) RuO_2/CNT in Figure 3.4, (a and d) DC, (b and e) RC 2.6 V and (c and f) RC. Scale bars represent 2 µm.

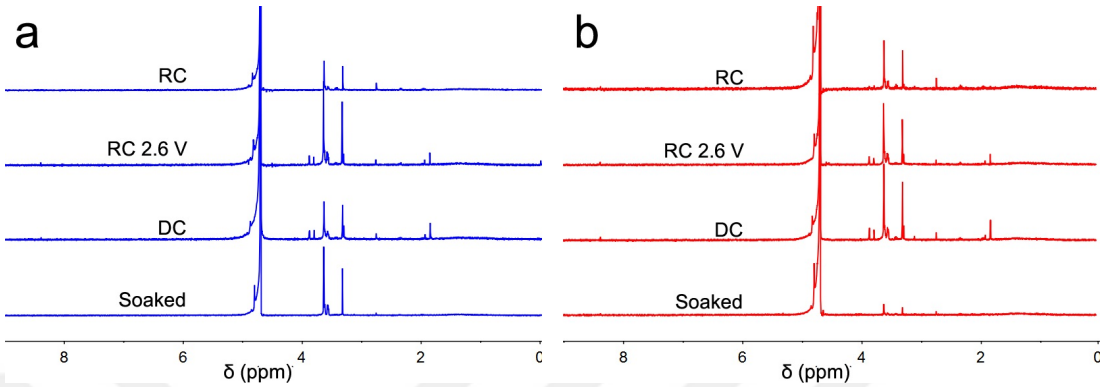

Figure 3.8: ^{1}HNMR spectra of the stepwise cycled (a) CNT and (b) RuO_2/CNT in Figure 3.4. ^{1}H chemical shifts (δ) of HDO, tetraglyme, acetate and formate are observed at 4.78, 3.35-4, 1.92 and 8.46 ppm [49], respectively, compatible with the XPS results.

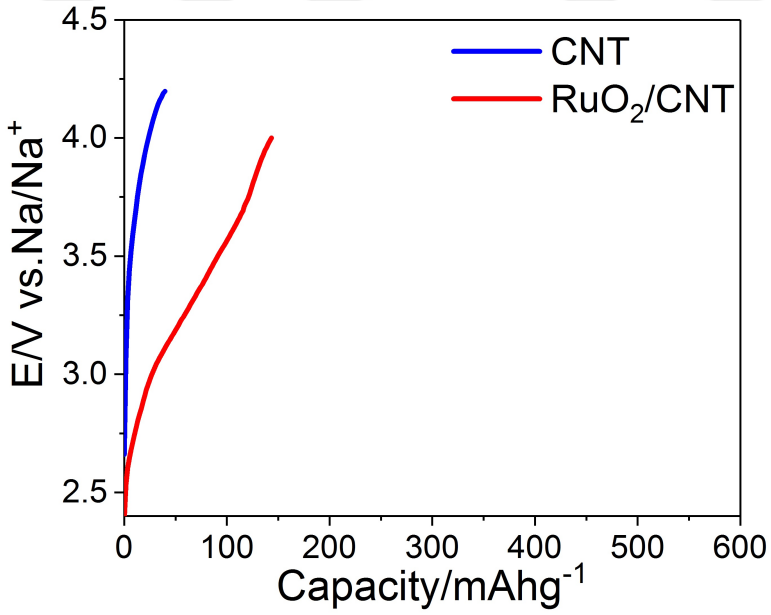

Figure 3.9: Galvanostatic charge of fresh CNT and RuO_2/CNT cathodes without pre-discharge. No significant plateau is observed in the charging curves of CNT and RuO_2/CNT up to 4.2 and 4 V, respectively, indicating that the plateaus observed in charging curves of cathodes in Figure 3.1 and Figure 3.13 are not corresponding to electrolyte decomposition.

In the next step, we analyzed the identity, crystallinity and morphology of DC product in CNT and RuO_2/CNT cathodes. The appearance of an intense Raman band at 1156 cm^{-1} in Raman spectra of DC samples, which was absent in the RC cathodes, confirmed NaO_2 deposition as the main product during ORR and its decomposition during OER (Figure 3.11). The effect of RuO_2 catalyst on the crystallinity of NaO_2 discharge product was explored by X-ray diffraction (XRD) on pristine, DC and RC cathodes (Figure 3.10a). The patterns of DC cathodes consist of mainly two peaks at 2θ= 32.5° and 46.6° relating to (200) and (220) reflections of NaO_2 (ICSD 98-008-7177), respectively, which vanish in the RC cathodes. However, the crystallinity of NaO_2 considerably differed in DC CNT and DC RuO_2/CNT. According to (200) reflection peak area of NaO_2, the relative amount of crystalline NaO_2 in DC RuO_2/CNT cathode was ∼31% of that in DC CNT cathode. Estimating the same quantity of total NaO_2 in both DC cathodes (both cathodes were discharged to 1.5 mAh), it turned out that ∼69% of NaO_2 is deposited in non-crystalline form by the effect of RuO_2 catalyst.
In order to further probe the NaO_2 morphology change triggered by RuO_2 catalyst, DC cathodes were explored by SEM and TEM. The DC CNT cathode contained well defined micron-sized cubic NaO_2 (Figure 3.10b and d), compatible with the observation of Hartmann et al. [12]. Instead, drastic morphological changes were observed in DC RuO_2/CNT with the formation of film-like NaO_2 without any cubic particles (Figure 3.10c and e). TEM image of DC CNT cathode clearly shows bulk NaO_2 particle anchoring on CNTs with clean side walls (Figure 3.10f and 3.12). The crystalline nature of these particles was further approved by the selected area electron diffraction (SAED) pattern (Figure 3.12b), in which all the diffraction d-spacing values can be assigned to NaO_2 (ICSD 98-008-7177). This feature was distinguished from NaO_2 observed in DC RuO_2/CNT, in which a conformal NaO_2 film was observed on cathode without any exposed bare electrode surface left (Figure 3.10g and 3.12). The high resolution TEM (HRTEM) image (Figure 3.10h) clearly indicates the amorphous nature of the deposited NaO_2 film, which was also confirmed by observing no diffraction from NaO_2 in SAED pattern of DC RuO_2/CNT (Figure 3.12d). The NaO_2 deposited during DC was completely decomposed after RC and the cathodes preserved their original morphology after the first DC and RC (Figure 3.7c and f).

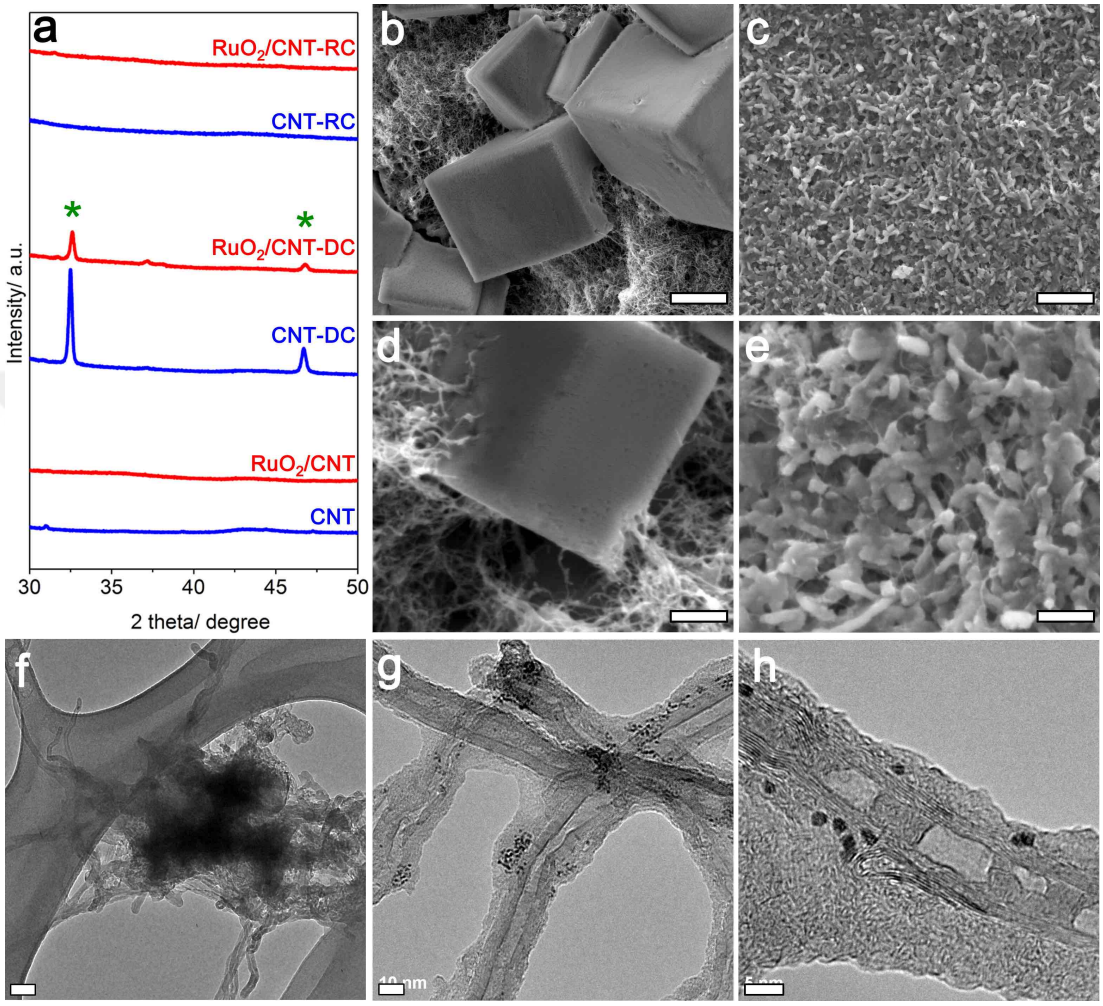

Figure 3.10: NaO_2 crystal and morphology characterization on CNT and RuO_2/CNT. (a) XRD patterns of CNT (blue) and RuO_2/CNT (red) at different states of: as prepared (bottom), first discharged (DC, middle) and first recharged (RC, up), with a limited capacity of 1.5 mAh. The symbol of * denotes NaO_2 reflection. (b-e) SEM images of CNT-DC (b and d) and RuO_2/CNT-DC (c and e). Scale bars indicate (b and c) 2 µm and (d and e) 500 nm. (f-h) TEM images of DC (f) CNT and (g and h) RuO_2/CNT cathodes. Scale bars indicate (f) 50 nm, (g) 10 nm and (h) 5 nm.

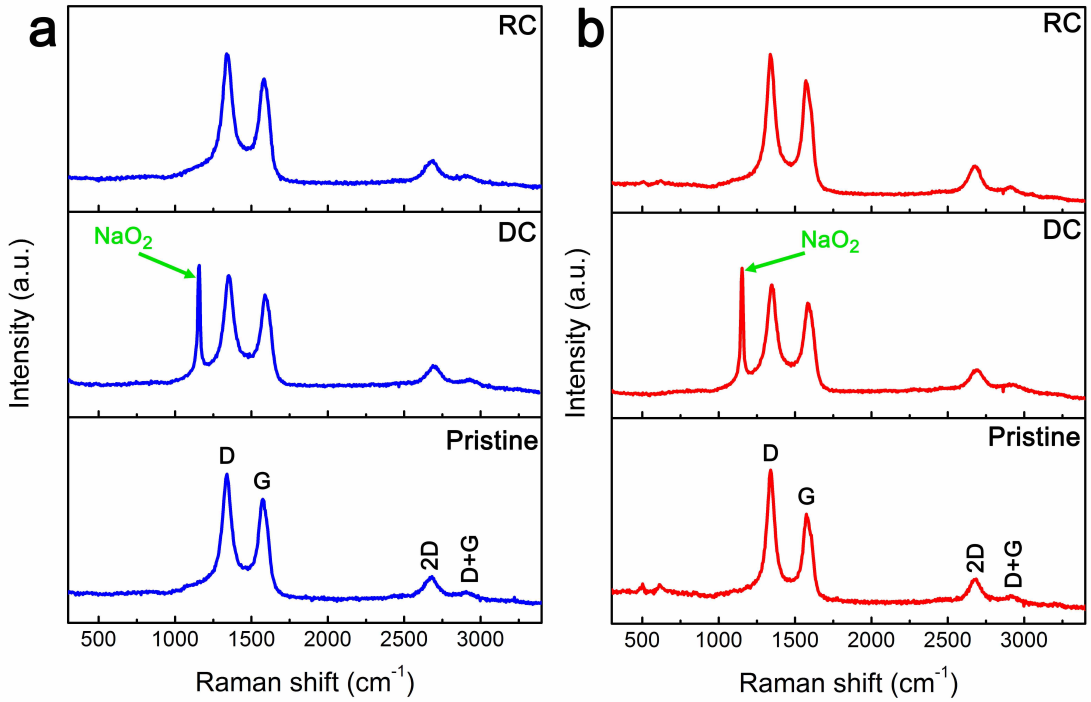

Figure 3.11: Raman spectra of pristine, DC and RC (a) CNT and (b) RuO_2/CNT. The presence of a sharp signal at 1155 cm^{-1} in DC spectra which is corresponding to the O-O stretch bonding of NaO_2 and its absence in RC spectra demonstrates NaO_2 deposition as the main discharge product and its decomposition during RC [12].

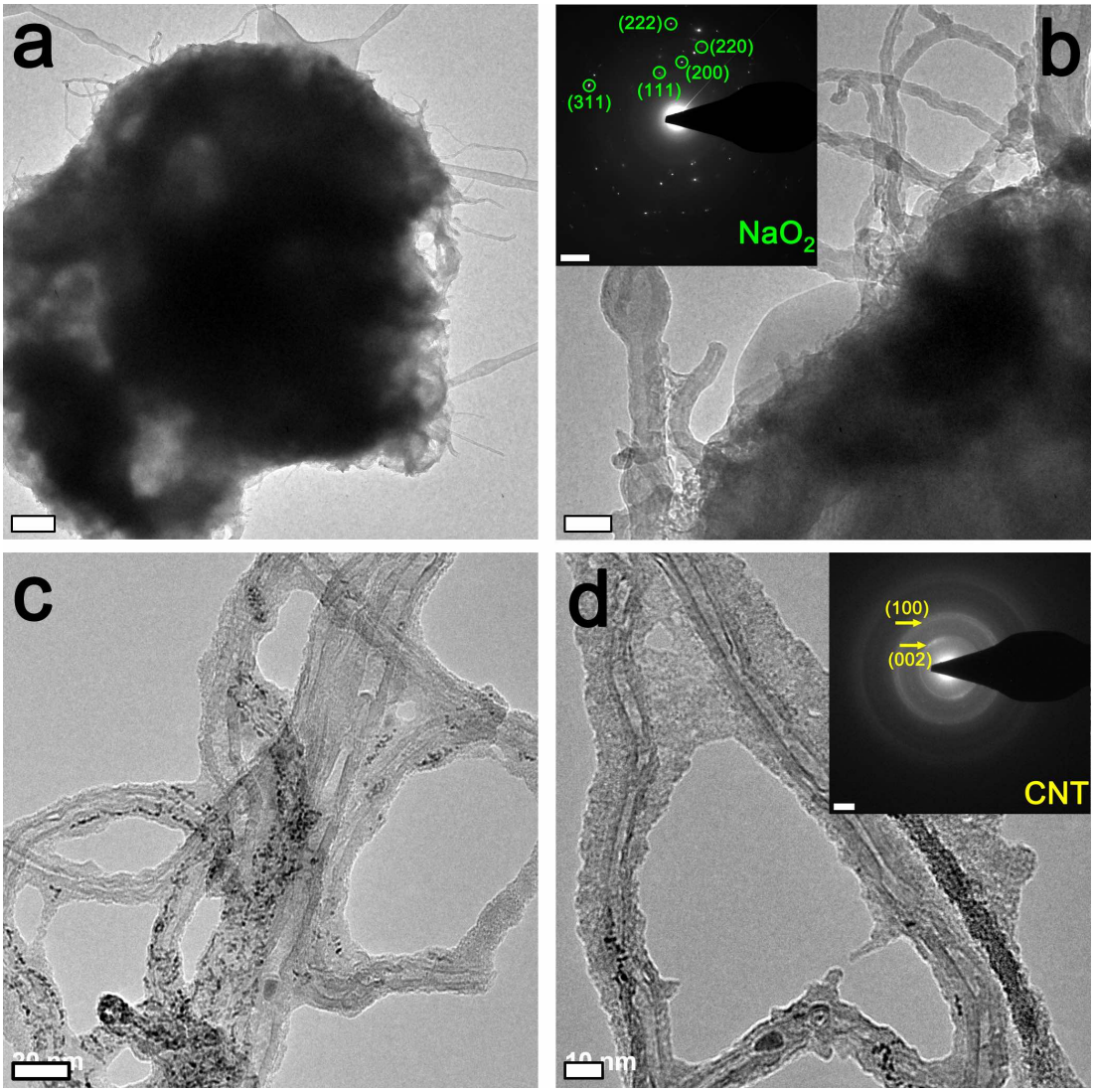

Figure 3.12: TEM images and electron diffraction patterns of (a, b) DC CNT and (c, d) DC RuO_2/CNT cathodes. Scale bars indicate (a) 200 nm, (b) 50 nm, (c) 20 nm, (d) 10 nm and (inset b and d) 2 nm^{-1}.

To address the differences in electrochemical response of CNT and RuO2/CNT during DC and RC, we carefully assessed the effects of operating parameters on the cells behavior at a limited cut off capacity (1000 $mAhg^{-1}$). Although the average DC potential for full capacity measurements (Figure 3.1b) was quite similar for both cathodes (∼2.05 V), RuO_2/CNT provided higher DC potential (2.084

V) than CNT (2.023 V) in the limited capacity measurement (Figure 3.13a), indicating improved kinetics in the initial state of ORR due to high electrocatalytic activity of RuO_2 NPs. According to Yilmaz et al., the passivation of catalyst surface by 3-4 layers of discharge product in the beginning step of DC results in the decreased DC potential of RuO_2/CNT catalyst during ORR [49]. Similar to full capacity measurements (Figure 3.1b), the limited capacity measurements also exhibited roughly three different charging plateaus (Figure 3.13a). For NaO_2 decomposition (region (i)), a negligible value of 23 mV reduction in charging potential was found for RuO_2/CNT compared with CNT (Figure 3.13a inset), which can be interpreted according to structural and morphological differences of NaO_2 on the two cathodes (Figure 3.10). The morphology and structure of Li_2O_2 is one of the key factors in determining Li-O_2 battery performance and its effect on the cell behavior is well understood. Huang et al. reported an anomalous performance enhancement of Li-O_2 batteries in which Li_2O_2 films are formed by a heterogenous nucleation mechanism on $NiFeO_x$ nanofiber catalyst [68]. The capability of constructing a LiO_2 rich environment by catalyst resulted in the production of oxygen rich Li_2O_2 films with high electrode/electrolyte contact area which promoted significantly lower over potential than the defect free Li_2O_2 particles formed in the absence of catalyst. Yilmaz et al. proposed that poorly-crystalline Li_2O_2 film deposited by using RuO_2 NPs can be decomposed at lower over potential during OER than the typical Li_2O_2 toroidal particles [49]. By using RuO_2 catalyst, the electrical efficiency of their cell improved up to 73%, which was higher than that of catalyst free cathode providing 58%. Also, the lower charging over potential of non-crystalline Li_2O_2 is suggested to be due to facilitated mass and charge transport through amorphous Li_2O_2 compared with its crystalline form **??**. Although amorphous Li_2O_2 is still a wide band gap insulator, it shows 4 orders of magnitude higher electronic conductivity and 12 orders of magnitude higher ionic conductivity than crystalline Li_2O_2 which is due to the increased mobility and concentration of Li vacancies in amorphous Li_2O_2.

Interestingly, RuO_2/CNT charging plateau deviates from the lowest voltage region after the initial 35% RC capacity which is prior to that of CNT at ∼65%

RC capacity. This sudden and precipitous increase in charging potential is believed to be due to dissolution of initial NaO_2 discharge product through the $NaO_2 \longrightarrow Na^+ + O_2^-$ reaction, which the liberated O_2^- chemically attacks the electrolyte or carbonaceous cathode to form a series of side products, decomposing at higher potentials during RC [19]. Sayed et al. showed that smaller NaO_2 cubic particles (∼200 nm) experience a higher charging potential than bigger particles (∼3 µm), which is due to higher exposed area and increased side products formation in smaller NaO_2 particles [25]. The accelerated dissolution and side products formation of film NaO_2 compared to cubic crystalline particles in this study can be also correlated to the higher surface area of the film and also its poor crystallinity (Figure 3.10), which is in agreement with the higher thermodynamic stability of crystalline structure. Therefore, there is a competition among the facilitated electrochemical decomposition of film NaO_2 and accelerated chemical formation of side products in RuO_2/CNT during charge. Since the formation of side products is a time dependent chemical process, the effect of NaO_2/electrolyte exposure time on charging behavior of both cathodes was examined on the cells rested between DC and RC at OCV from 3 to 30 days. As shown in Figure 3.14, resting up to 30 days led to a systematic decrease of the charging capacity for the lowest voltage region. A similar trend was observed while performing DC/RC experiments with different current rates (Figure 3.15), in which the capacities for the lowest voltage region were maximum for the highest current densities (faster DC/RC). This behavior is in line with the results observed in the literatures showing time dependent chemical reactions during resting time of discharged NaO_2 cells, which affect the reversibility of pre-deposited NaO_2 by the formation of side products [25, 28]. Figure 3.13b shows that after 30 days resting, the plateau at lowest potential is completely vanished and the average RC potential for RuO_2/CNT (3.66 V) is remarkably lower than that of CNT (4.03 V). Hence, two major regimes can be identified in Figure 3.13c of average charging potentials versus resting spans. During the short resting times (between 0 and 7 days), higher charging potential increment was observed for RuO_2/CNT (0.53 V) compared to CNT (0.38 V) which is due to accelerated NaO_2 decomposition in RuO_2/CNT cathode in short times. Nevertheless, during longer resting times, the effect of NaO_2 dissolution is not very critical for RuO_2/CNT cathode and

its catalytic effect can be noticed by decomposing the side products at lower charging potentials compared to CNT. Sun et al. and Wu et al. reported tuning the properties (morphology, composition, structure) of NaO_x (NaO_2/Na_2O_2) discharge product in Na-O_2 batteries by Co_3O_4/CNT and m-RuO_2/B-rGO catalysts, respectively [58, 60]. The improved cells performance was attributed to the catalytic activity of the catalysts towards the electrochemical decomposition of NaO_x and Na_2CO_3. However, the dissolution of NaO_2 during cell operation and the earlier deviation of charging potential from the lowest potential plateau compared to CNT was not considered carefully for Co_3O_4/CNT. It should be also noted that no NaO_2 discharge product was observed in DC m-RuO_2/B-rGO cathode. According to our results, the effect of catalyst for tuning morphology and structure of NaO_2 in Na-O_2 batteries is attenuated by the noxious NaO_2 dissolution during cell operation or resting.

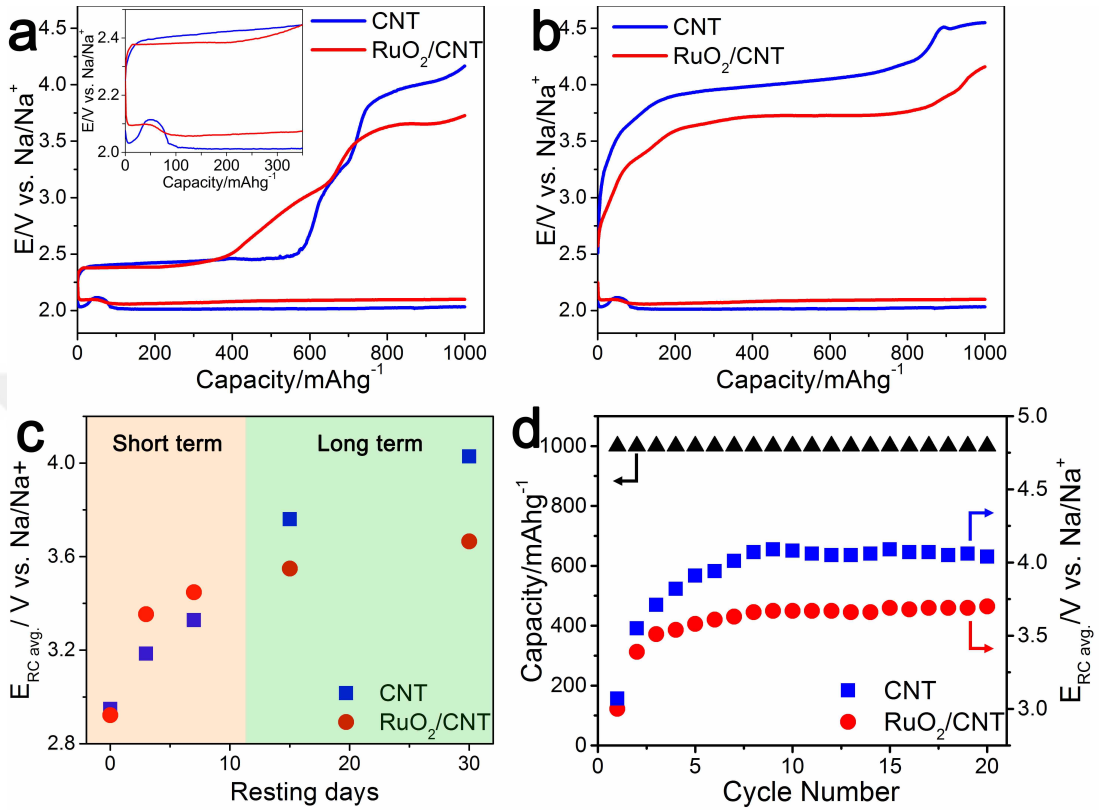

Figure 3.13: Electrochemical measurements of CNT and RuO_2/CNT. (a and b) Galvanostatic DC/RC of RuO_2/CNT and CNT at 100 mAg^{-1} with a limited capacity of 1000 $mAhg^{-1}$ (a) without and (b) with 30 days resting between DC and RC. Inset in (a) shows the magnified graph of the beginning 350 $mAhg^{-1}$ of DC, in which NaO_2 decomposes at lower potential in RuO_2/CNT compared to CNT during OER. (c) The results of charging potentials versus resting spans for the samples rested 0-30 days between DC and RC, extracted from Figure 3.14. The time domain is divided to short and long terms, in which RuO_2/CNT cathode exhibits higher and lower RC average potentials, respectively. (d) Cycling performance of CNT and RuO_2/CNT with a current density of 100 mAg^{-1} and limited capacity of 1000 $mAhg^{-1}$. The black triangles (linked to the left y-axis) show the capacity of both cathodes during cycling and the blue squares and red circles (linked to the right y-axis) indicate the average RC potential during cycling for CNT and RuO_2/CNT, respectively.

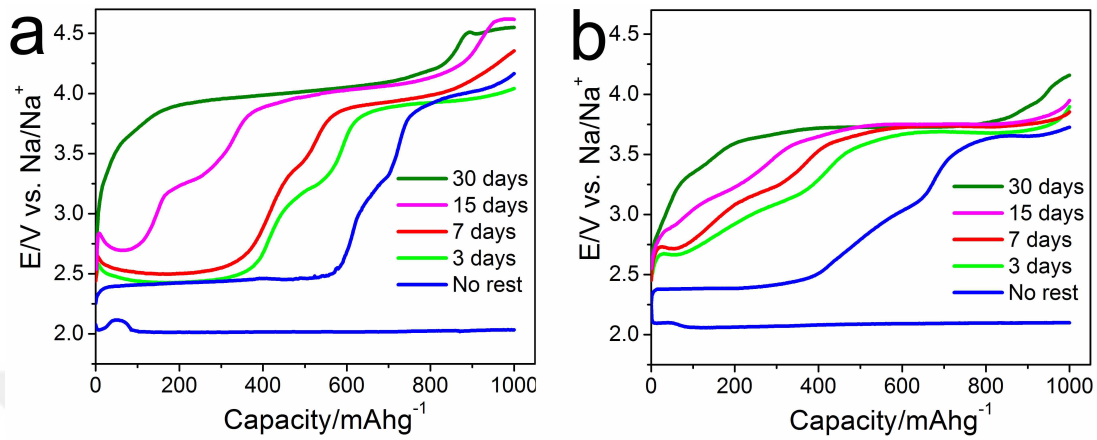

Figure 3.14: Galvanostatic DC/RC curves of (a) CNT and (b) RuO_2/CNT at 100 mAg^{-1} and limited capacity of 1000 $mAhg^{-1}$, with 0-30 days resting between DC and RC. Obviously, the relative length of lowest potential plateau decreases by increasing resting days, indicating that the side products formation by NaO_2 degradation is a time dependent chemical process.

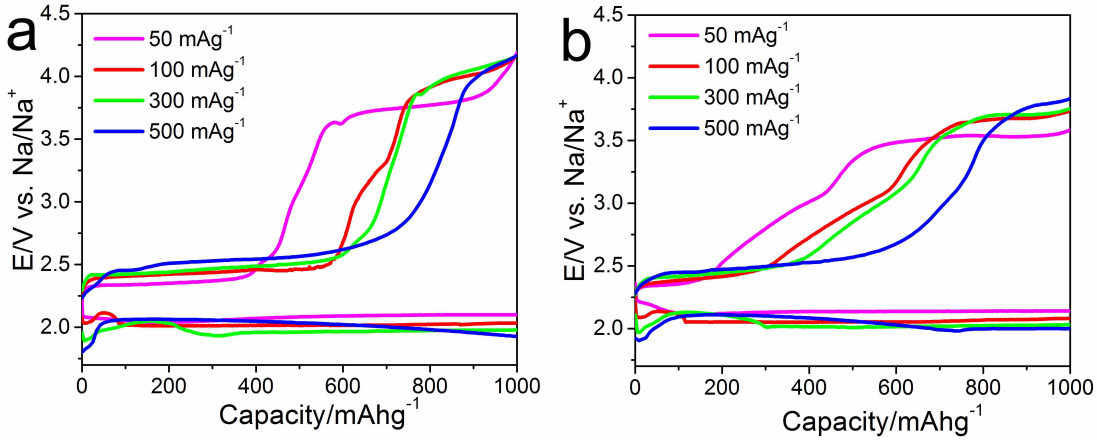

Figure 3.15: Galvanostatic DC/RC measurements of (a) CNT and (b) RuO_2/CNT at different current rates of 50-500 mAg^{-1} with a limited capacity of 1000 $mAhg^{-1}$. It is apparent that by increasing the current rate, the relative lengths of lowest potential plateaus corresponding to NaO_2 decomposition increase. This may be due to the shorter NaO_2/electrolyte exposure time at higher current rates and consequently decreased amount of decomposition side products.

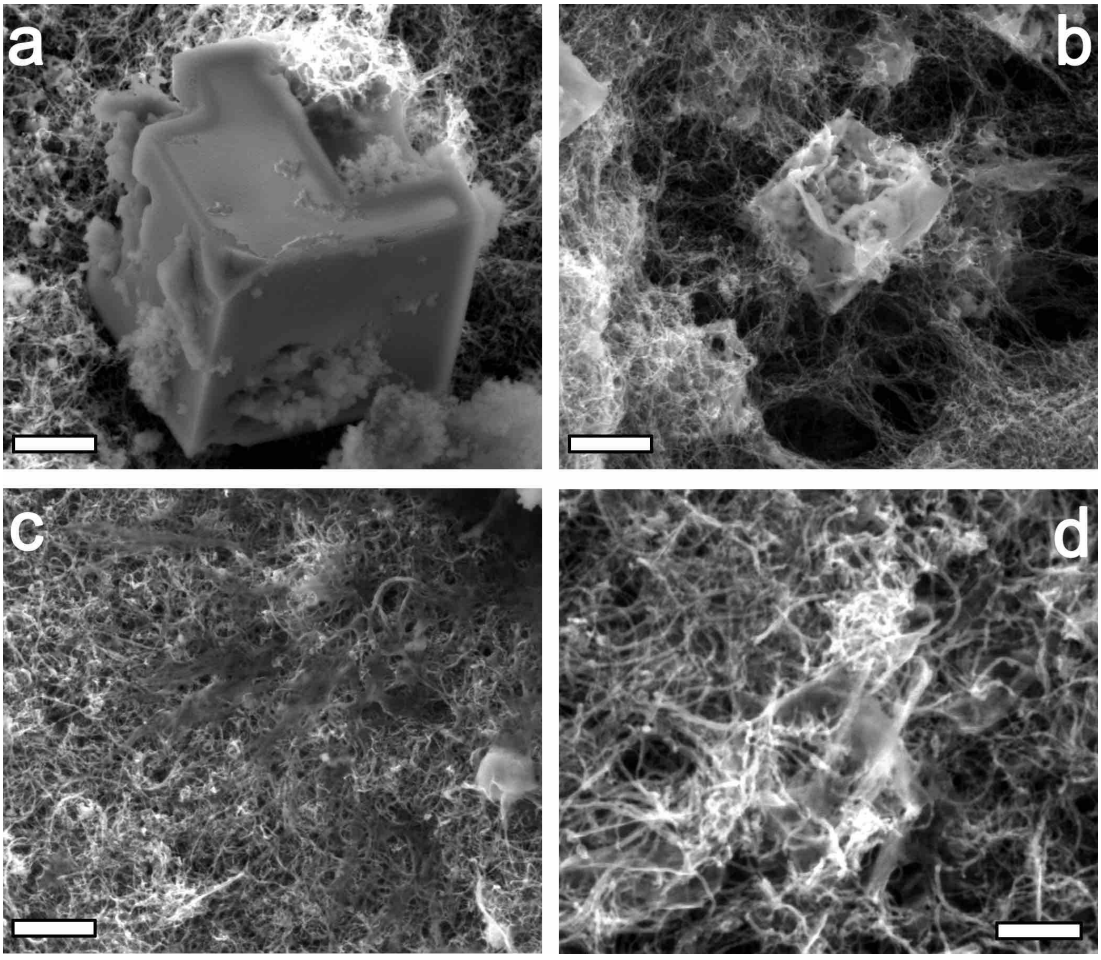

Figure 3.16: SEM images of (a, b) CNT and (c, d) RuO_2/CNT cathodes discharged to 1000 $mAhg^{-1}$ and rested for 30 days. The scale bars indicate (a-c) 1 µm and (d) 500 nm. The roughen surface of NaO_2 is indicative of surface side reactions during resting time without applying any current in OCP. The effect of side reactions is more severe on the morphology of smaller cubes in (b) and film NaO_2 in (c, d) due to their higher exposed surface area to the electrolyte.

The cycling performance of RuO_2/CNT and CNT cathodes was also examined using a cut-off capacity of 1000 $mAhg^{-1}$ at 100 mAg^{-1} current density (Figure 3.13d and 3.17). An increasing trend was found in the charging potential of both cathodes during the beginning 5 cycles, which is due to the accumulation of side products during cycling as reported by Black et al. [67]. During the following

cycles, RuO_2/CNT showed a stable charging potential at ~3.7 V which is much smaller than that of CNT at ~4.05 V. By investigating the cycled cathodes with SEM, it can be seen that accumulation of side products in CNT cathode is more pronounced than RuO_2/CNT after 20 cycles, which is further confirmed by XPS C^{1s} spectra of the cycled cathodes, in which CNT shows higher ratio of functional decomposition groups: C-C compared with RuO_2/CNT (Figure 3.18).

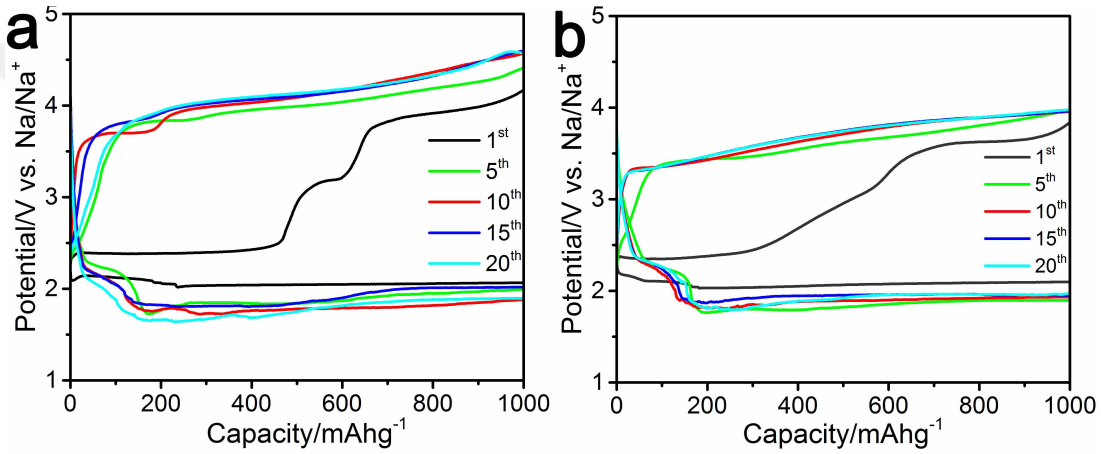

Figure 3.17: Cycling performance of (a) CNT and (b) RuO_2/CNT with a limited capacity of 1000 $mAhg^{-1}$ at a current density of 100 mAg^{-1}.

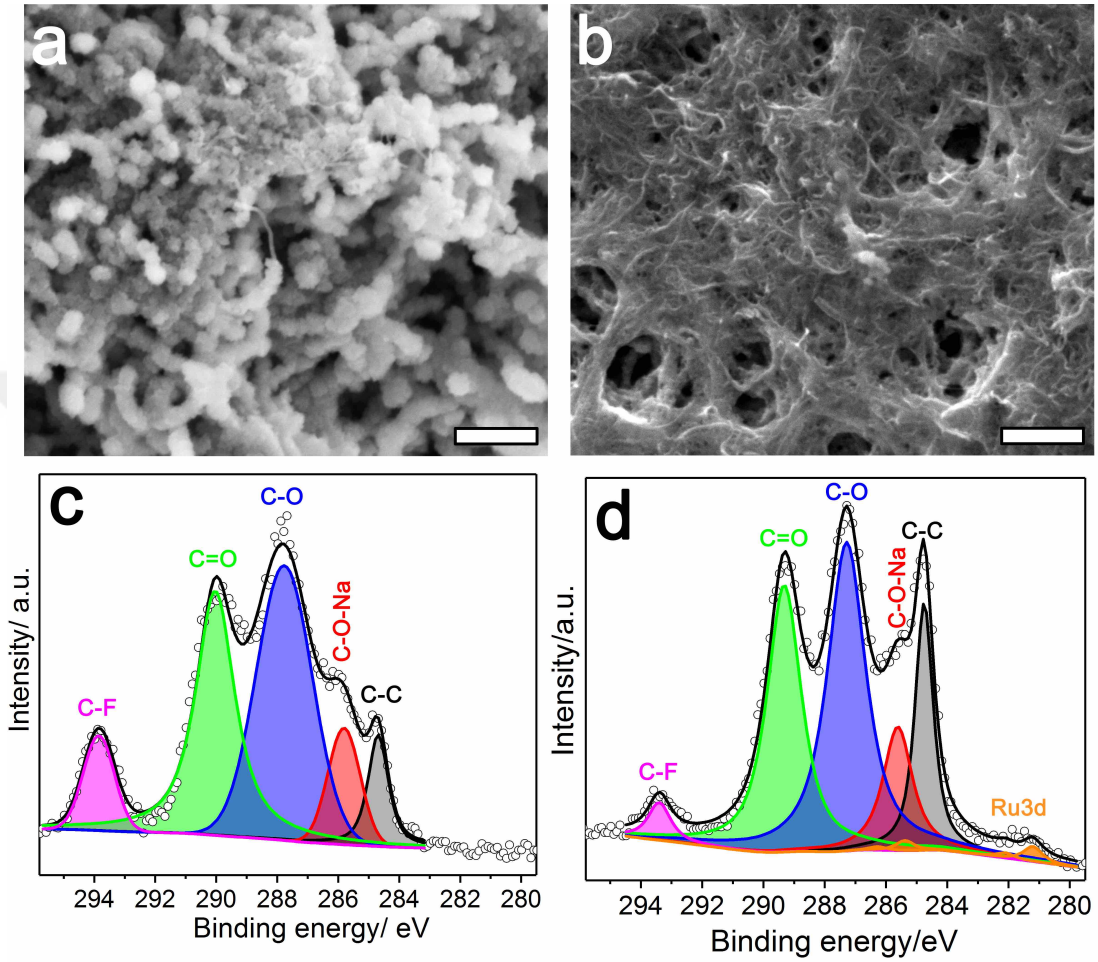

Figure 3.18: (a and b) SEM images and (c and d) XPS C^{1s} spectra of (a and c) CNT and (b and d) RuO_2/CNT after 20 DC/RC cycles. Scale bars in (a and b) represent 500 nm. According to the SEM images, the accumulation of side products on the surface of CNT is more severe than RuO_2/CNT after 20 cycles, which is further approved by the XPS C^{1s} spectra, in which the ratio of C-C: functional groups signal is lower in CNT than that of RuO_2/CNT. Therefore, it can be realized that RuO_2 actively contributed to the decomposition of side products during cycling.

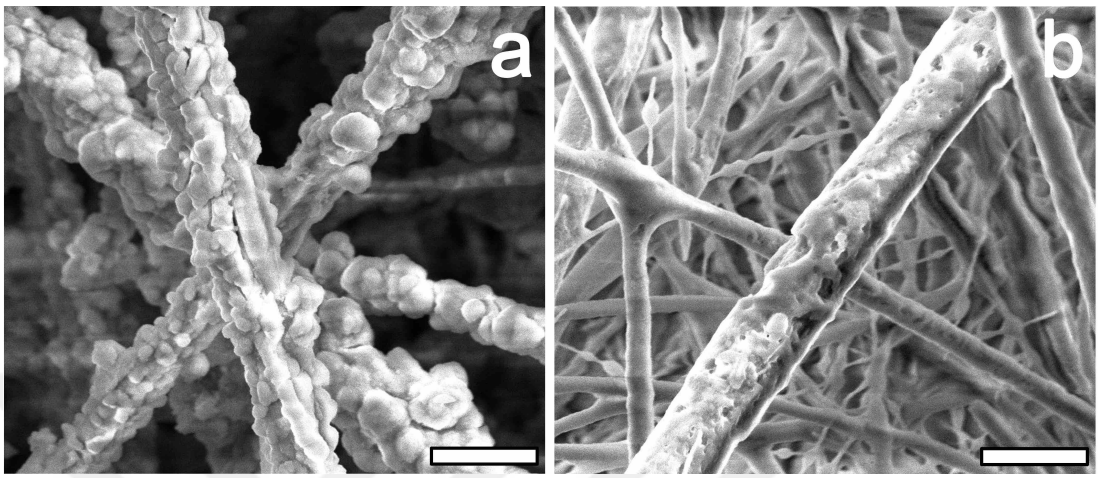

Figure 3.19: SEM images of the separators after 20 DC/RC cycles, (a) CNT and (b) RuO_2/CNT. The scale bars represent 2.5 µm. The separators surface coverage by some products is indicative of the presence of dissolved species in the electrolyte, as a result of O_2^- dissolution, which can migrate and deposit on different cell components.

Combining all of the experiments and inspired by the above mentioned references, we demonstrate the role of RuO_2 NP catalyst on Na-O_2 battery electrochemistry. The following ORR mechanism can be confirmed during DC:

$O_2 + * \longrightarrow O_2*$ (1)

$O_2* + e^- \longrightarrow O_2^-$ (2)

$Na^+ + O_2^- \longrightarrow NaO_2$ (3)

Where the asterisk symbol (*) demonstrates active surface sites. Due to the high affinity of O_2* towards RuO_2 NPs, steps 1-3 and the following lateral growth of NaO_2 occur in the proximity of RuO_2 in the beginning of DC. Also, the relatively strong adsorption of O_2* to RuO_2 NP ($RuO_2 \ldots O_2*$) suppresses a decent Na-O_2* binding, therefore structural defects (like Na vacancies) in the final NaO_2 can be expected resulting in a poorly crystalline product. As a result of covering the whole surface of RuO_2 NP catalyst with NaO_2 in the following DC process, the DC over-potential increases as the lateral growth continues on bare CNT surface. It is noteworthy that in the absence of RuO_2 catalyst, steps 1 and 2 take place apart from step 3, linked by O_2^- migration through the electrolyte on the already

precipitated NaO_2 (Figure 3.20) which is known as the solution mediated route and is responsible for the formation of micron sized insulating NaO_2 cubes [23]. It is distinct from the surface mediated route happening in the presence of RuO_2 catalyst, in which the film like coating morphology is a result. In comparison with Li-O_2 batteries, the unique superoxide chemistry in Na-O_2 batteries urges inevitable dissolution during storing time after DC. According to our results, the higher contact area of film NaO_2-electrolyte and also its structural defects exert more pronounced ionization and side products formation compared with the crystalline cubic NaO_2 particles.

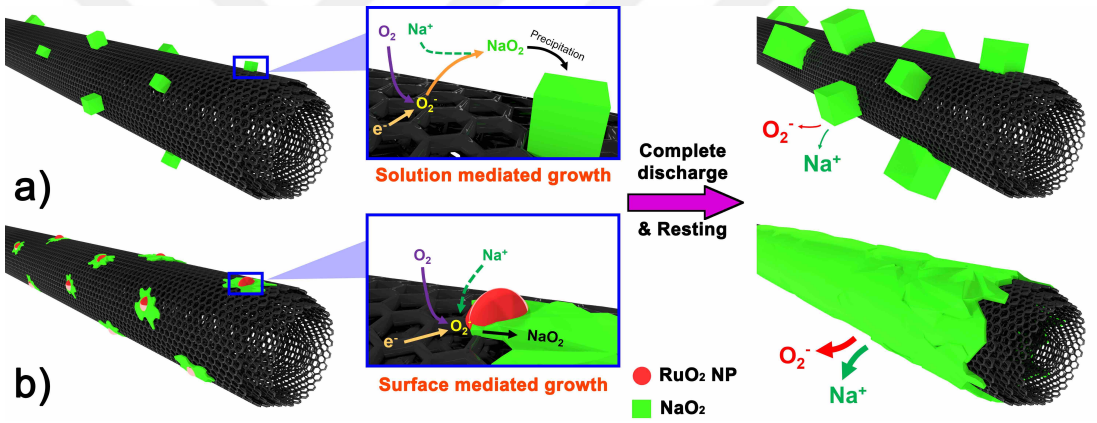

Figure 3.20: Schematic illustration of NaO_2 nucleation and growth on (a) CNT and (b) RuO_2/CNT cathode.

3.2 RuO_2/Mn_2O_3/CNF Cathode

The morphological and structural evaluations of MC, RC and RMC are performed by SEM (Figure 3.21). The as electrospun CNF exhibits fibrous structure with smooth surface and mean diameter of 255 nm (176- 382 nm) (Figure 3.21a). However, drastic morphological changes were observed after Mn_2O_3 deposition on CNF (Figure 3.21b). Although the CNF framework remains unchanged in MC sample, the deposition of Mn_2O_3 nano-rods turns the structure to a 3D porous platform, which become quite desirable for RuO_2 nanoparticle decoration in the

next step. After RuO_2 deposition, the change in Mn_2O_3 nano-rods diameter can be recognized in SEM images of RMC samples (Figure 3.21c) when compared to MC. Furthermore, the surface morphology of RMC in Figure 3.21c exhibits no agglomeration of RuO_2, showing that the RuO_2 nanoparticles were effectively deposited on Mn_2O_3 nano-rods. In order to realize the function of porous Mn_2O_3 nano-rods framework in the second hydrothermal step, as electrospun pristine CNF was used for RuO_2 deposition to make RC (Figure 3.21d). It can be seen

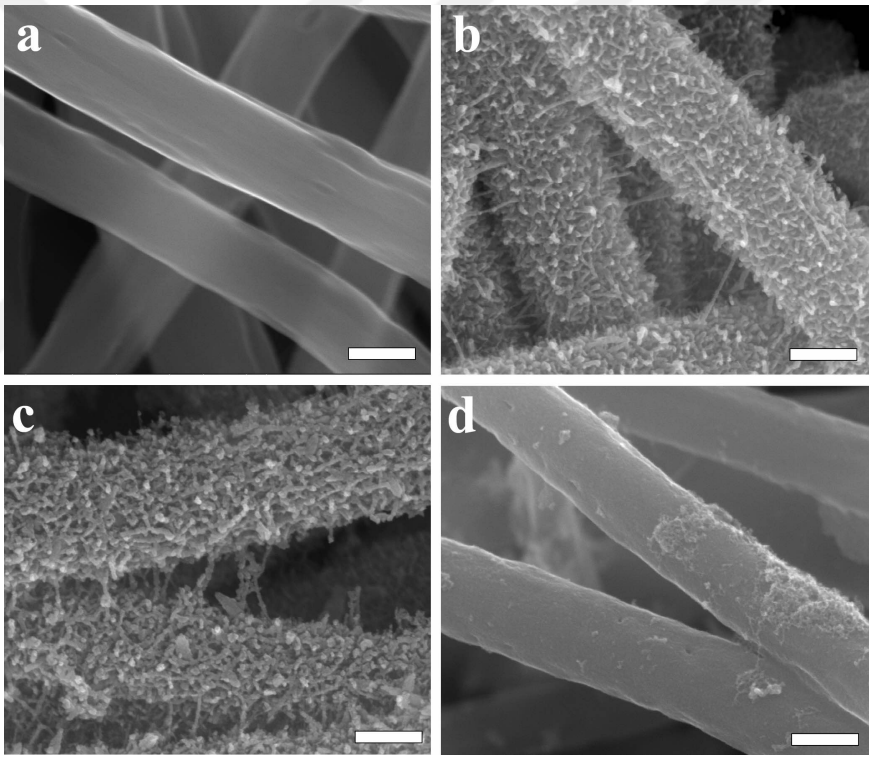

Figure 3.21: SEM images of (a) CNF, (b) MC, (c) RMC and (d) RC (Scale bars, 200 nm).

that in the absence of Mn_2O_3 nanorods, RuO_2 agglomerates are dominating in this sample. This behavior demonstrates that Mn_2O_3 nanorods act as trapping network to anchor individual RuO_2 nanoparticles which results in the uniform distribution of them in the structure.

TEM has been exploited to further investigate the nanostructure of MC, RMC and RC, as shown in Figure 3.22 and 3.23. The TEM and high resolution TEM

(HRTEM) imaging revealed that a large number of Mn_2O_3 nano-rods are grown upright on CNF in MC, making an open porous 3D nano-structure (Fig 3.22a and b and 3.23a). The selected area electron diffraction (SAED) pattern of MC shows the characteristic diffraction rings attributed to the (004), (044) and (226) planes, indicating the crystalline nature of Mn_2O_3 nano-rods. The TEM images of RMC

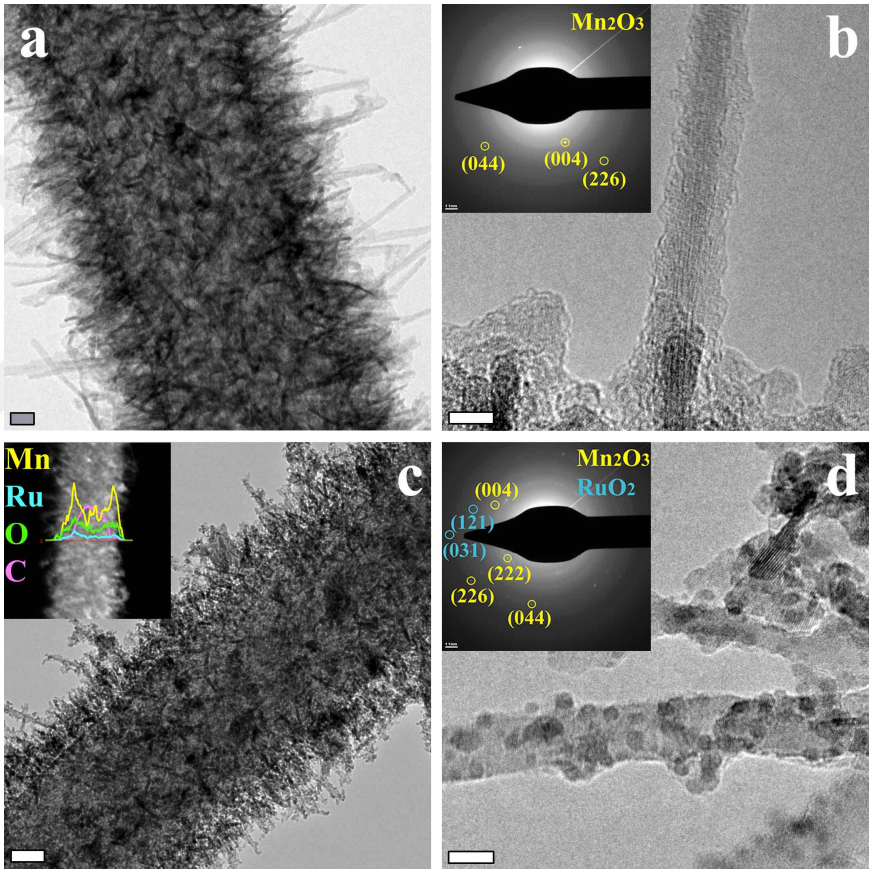

Figure 3.22: TEM (a and c) and HRTEM (b and d) images of MC (a and b) and RMC (c and d). Inset in b and d is the corresponding SAED pattern. Inset in c represents the EDS elemental line scan of RMC (Scale bars, a: 50 nm, b and d: 5nm, c and inset: 50 nm).

show that RuO_2 nanoparticles with the mean size of 1.57 nm are uniformly distributed on Mn_2O_3 nano-rods without any agglomeration and pore clogging, further confirming the trapping function of Mn_2O_3 nano-rods in the structure

(Figure 3.22c, d and 3.23b). The formation of hierarchical RMC was further examined by high angle annular dark field scanning TEM (HAADF-STEM) images (Figure 3.23b) which yielded a clear contrast between RuO_2 nanoparticles and Mn_2O_3 nano-rods. The elemental EDS line scan results (Figure 3.22c inset) show the presence of O, Mn, Ru and C in the structure. The relative positions of these elements indicate that O, Mn and Ru were across the whole structure, therefore,

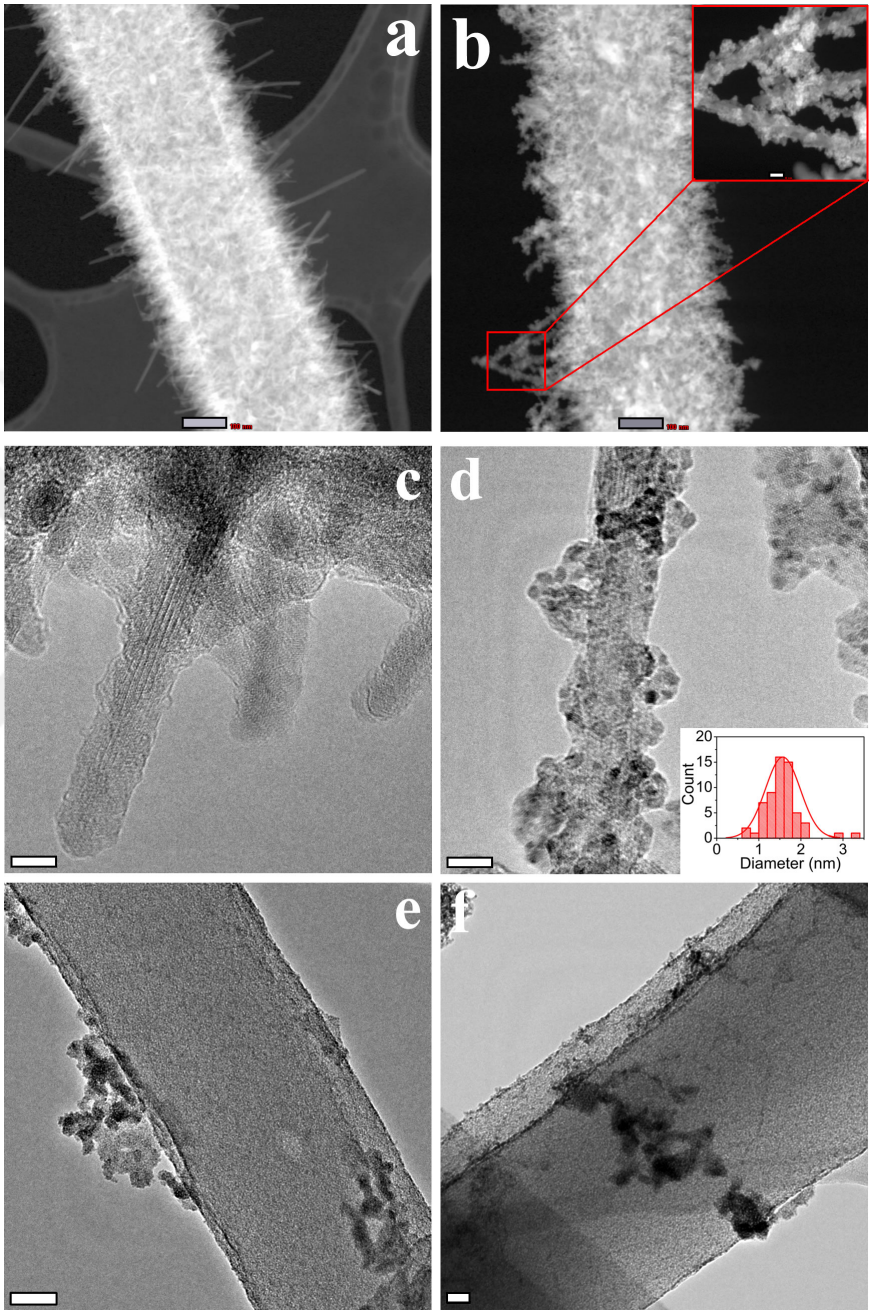

Figure 3.23: HAADF-STEM images of (a) MC and (b) RMC. Inset in b is higher magnification STEM image of the selected rectangular area. Additional HRTEM images of (c) MC and (d) RMC. Inset in d represents the particle size distribution of RuO_2 nanoparticles on Mn_2O_3 nano-rods. (e and f) TEM images of RC (Scale bars, a and b: 100 nm, b inset: 20 nm, c and d: 5 nm, e: 50 nm and f: 20 nm).

RuO_2/Mn_2O_3 has grown on the CNF core. Furthermore, SAED pattern of RMC (Figure 3.22d inset) consists of characteristic diffraction rings of (121) and (031) planes attributed to RuO_2 and those of Mn_2O_3. The agglomerating nature of RuO_2 nanoparticles was also observed in more detail in TEM images of RC (Figure 3.23e and f).

The crystallinity of the samples was further analyzed by XRD (Figure 3.24a). The XRD pattern of CNF shows a broad peak at $2\theta = 25°$ corresponding to the (002) plane of graphitic carbon. In the diffraction patterns of MC and RMC samples, the peaks at $2\theta = 33°$, 38.2°, 55.4° and 65.8° are corresponding to (222), (004), (044) and (226) planes of Mn_2O_3 (ICSD 98-003-3647), respectively. It can be realized that Mn_2O_3 gets more crystalline in RMC sample compared to MC sample which can be owing to the second hydrothermal step for RuO_2 deposition. Also, no obvious peaks relating to RuO_2 were observed in the patterns of RC and RMC samples which is because of minor amount and small crystal size of RuO_2. Figure 3.24b shows the Raman spectra of the samples, in which there are two main peaks of CNF including D band at 1351 cm^{-1} related to the phonons with A^{1g} symmetry and G band1584 cm^{-1} corresponding to the E^{2g} phonon of sp^2 carbon atoms [69]. The Raman spectra of MC and RMC samples exhibit three bands at 500 cm^{-1}, 560 cm^{-1} and 620 cm^{-1} which are corresponding to the asymmetric stretching of bridging oxygen species (Mn-O-Mn) and symmetric stretch

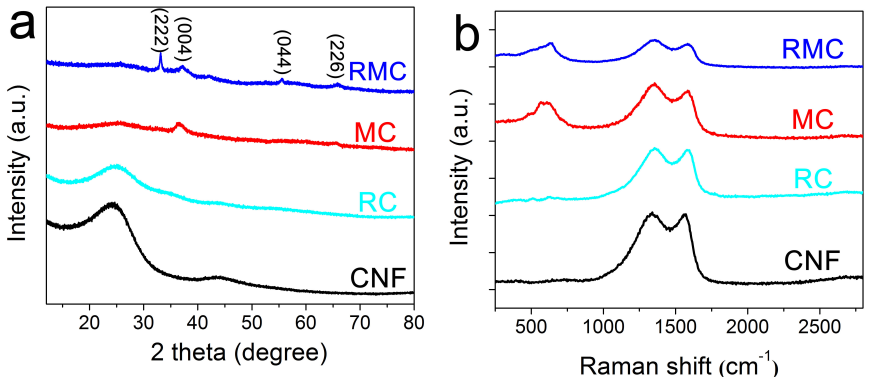

Figure 3.24: (a) XRD patterns and (b) Raman spectra of CNF, RC, MC and RMC.

of Mn_2O_3 groups [70]. The Raman spectrum of RC shows two peaks at 520 cm^{-1} and 631 cm^{-1} which are related to the first order E_g and A_{1g} phonon bands of rutile RuO_2 [71]. However, since the peaks of RuO_2 and Mn_2O_3 coincide in the same spectrum region, there is no obvious peak of RuO_2 in RMC spectrum. In order to show the excellent synergistic effect in RMC sample, the prepared materials were utilized in Na-O_2 cells as the cathode electrodes. Galvanostatic discharge/charge tests at 0.05 $mA.cm^{-2}$ (Figure 3.25a) indicate the higher specific capacity for RMC (9352$mAh.g_{carbon}^{-1}$) compared with CNF (1395 $mAh.g_{carbon}^{-1}$), MC (3108 $mAh.g_{carbon}^{-1}$) and RC (4859 $mAh.g_{carbon}^{-1}$) at the end of discharge with the cutoff potential of 1.5 V. The following charging profiles consist of two main plateaus at lower ($\sim$2.4 V) and higher ($\sim$4 V) potentials which are assigned to the decomposition of NaO_2 and the side products (mainly Na_2CO_3), respectively [19, 58]. According to the overall discharge/charge measurements, RMC not only exhibits higher specific capacity by promoting the formation and decomposition of NaO_2, it also facilitates side products decomposition during charge at lower potential (3.838 V) compared to CNF (4.226 V), MC (4.077 V) and RC (3.963 V). In order to have a better understanding of the nature of discharge product, Raman spectroscopy of the samples at the end of discharge was investigated (Figure 3.25b). The dominance of the Raman band at 1156 cm^{-1} confirms the deposition of NaO_2 as the main discharge product during ORR [12]. However, drastic morphological differences of deposited NaO_2 were observed between discharged CNF and the other discharged cathodes (Figure 3.25c-f). Figure 3.25c shows that micron-sized cubic NaO_2 particles are deposited at CNF cathode after discharge, compatible with the report of Hartmann et al [12]. By incorporating Mn_2O_3 and/or RuO_2 on CNF, no further cubic particle was observed on the discharged cathodes (Figure 3.25d-f), instead, the samples were buried under a conformal coating of NaO_2. This behavior is well understood in Li-O_2 batteries in which the morphology of Li_2O_2 discharge product is transformed from conventional toroidal particles to film coating by introducing catalyst on the surface of carbonaceous backbones [49, 72]. In fact, this change is ascribed to the favored adsorption energy of peroxide and superoxide species on the surface of catalyst as the discharge product nucleation spots and the following growth [73]. Therefore, the catalytic reaction can be performed throughout the entire 3D RMC structure

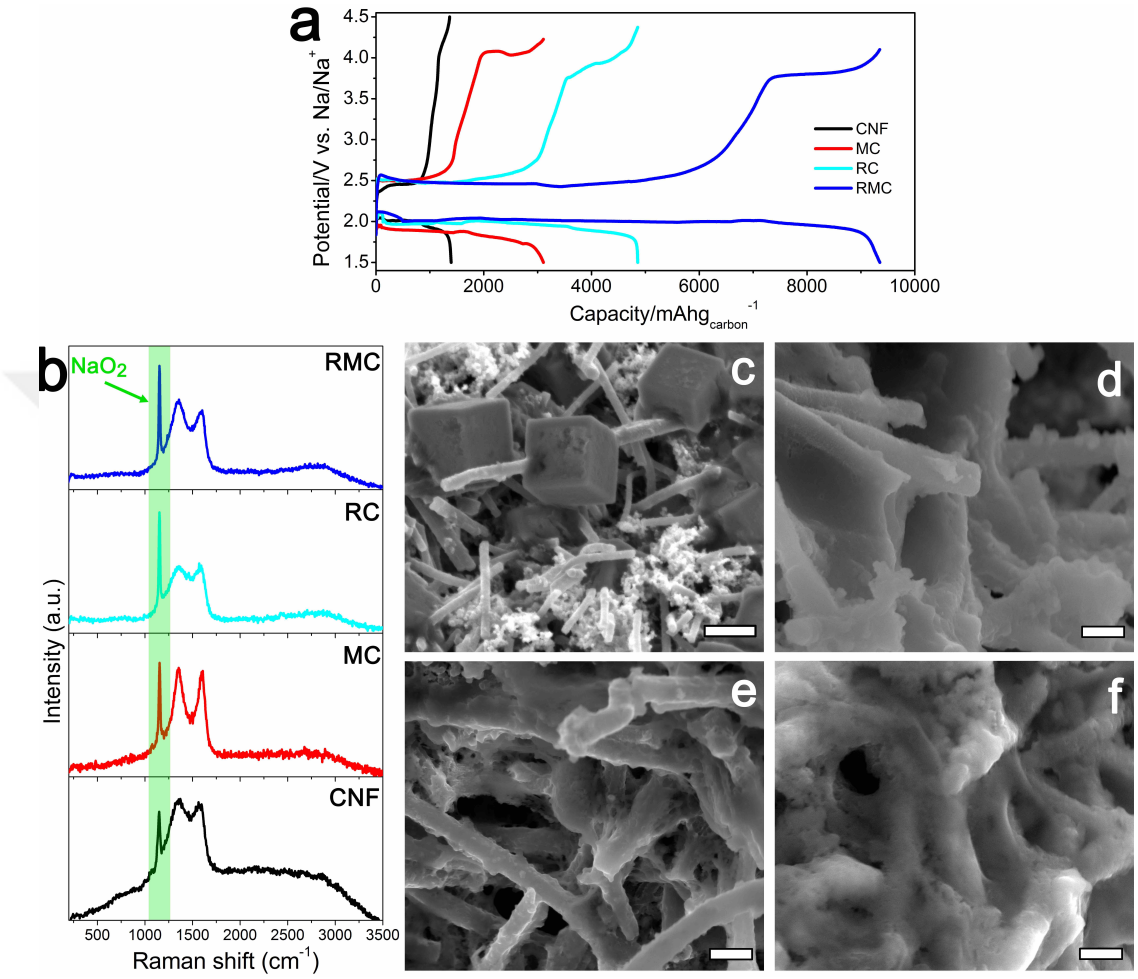

Figure 3.25: (a) Galvanostatic discharge/charge plots of CNF, MC, RC and RMC at a current density of 0.05 mA.cm^{-2}, (b) corresponding Raman spectra of the samples at the end of discharge. The dominance of the strong peaks in the Raman spectra at 1156 cm^{-1} (highlighted spectrum) indicates deposition of NaO_2 as the main discharge product at the end of discharge. SEM images of (c) CNF, (d) MC, (e) RC and (f) RMC discharged cathodes. Scale bars represent: (c) 1.5 µm and (d-f) 500 nm. Conformal distribution of NaO_2 on MC, RC and RMC indicates the catalytic reaction throughout the whole structures.

rather than only in some local regions as observed in CNF. There is no precipitate observed in the SEM images of the cathodes after charging, indicating that the cathodes have reversibly recovered their structures at the end of complete

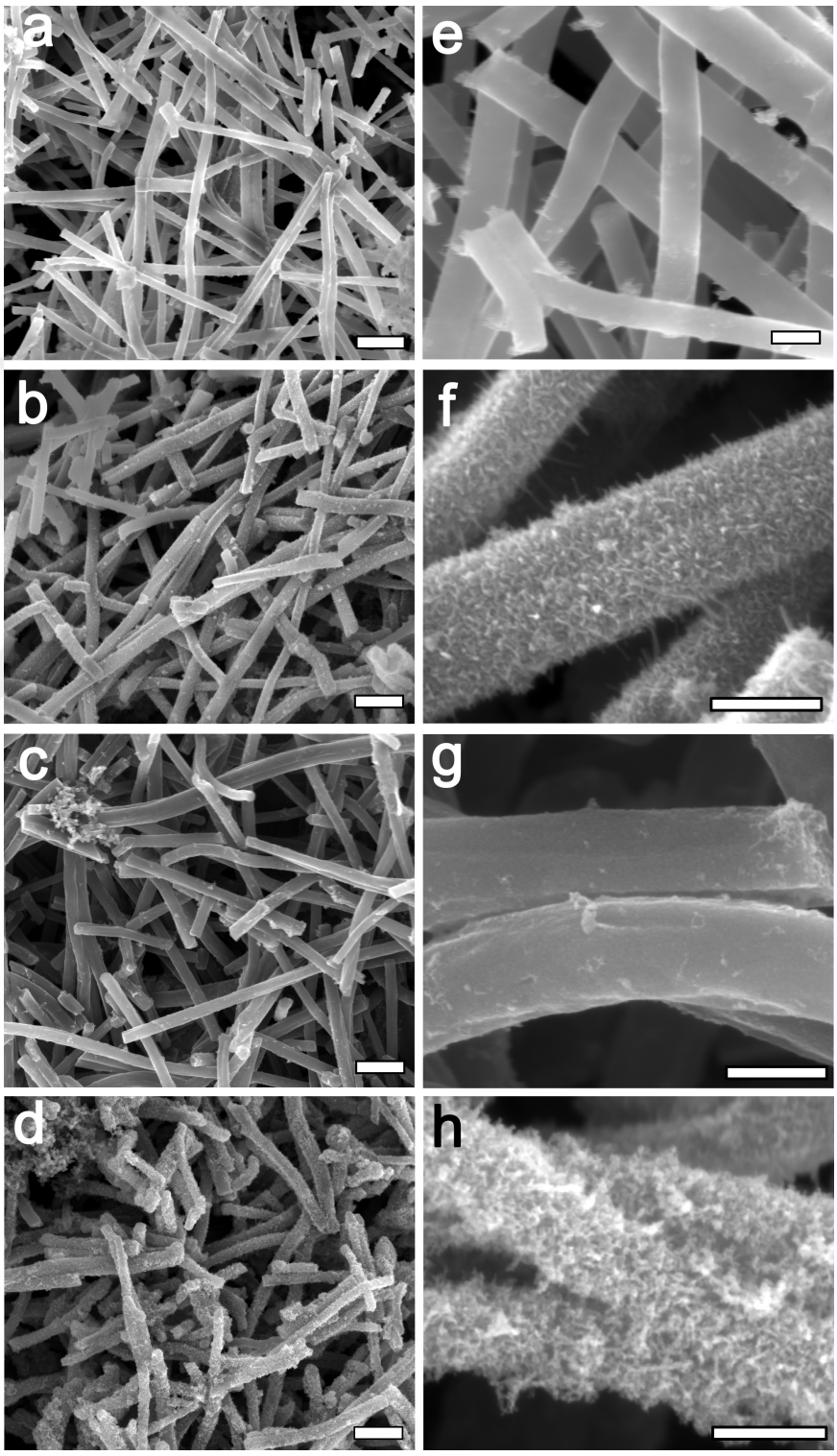

Figure 3.26: SEM images of charged CNF (a and e), MC (b and f), RC (c and g), and RMC (d and h) at low (a-d) and high (e-h) magnifications. Scale bars indicate: (a-d) 1 µm and (e-h) 250 nm.

discharge/charge cycle (Figure 3.26).

Chapter 4

SUMMARY

In summary, the effect of RuO_2/CNT catalyst on Na-O_2 battery electrochemistry/chemistry was studied. RuO_2/CNT actively contributed to the formation of a film like NaO_2 which is 69% less crystalline than the cubic NaO_2 particles deposited on CNT. It turned out that the physical distinctions among film and cubic particle NaO_2 severely influence their stability during resting spans between DC and RC and even during RC. The high electrode/electrolyte contact area of film NaO_2 and its lower crystallinity favors more dissolution, elevated side products formation and RC over-potential increment for RuO_2/CNT. On the other hand, RuO_2 catalyzes side products decomposition during OER which exerts 0.37 V lower RC over-potential for side products decomposition region compared to bare CNT. However, the catalyst could not actively catalyze the main cell reaction during charge ($NaO_2 \longrightarrow Na^+ + O_2 + e^-$) due to the accelerated side products formation from the coating like NaO_2 chemical decomposition. Therefore, the use of catalyst for tuning superoxide morphology and crystallinity in Na-O_2 batteries is denied and should be taken into account for the future applications.

Also, a highly effective 3D RuO_2/Mn_2O_3/CNF ternary composite has been prepared and used as the bi-functional electrocatalyst for ORR/OER in Na-O_2 batteries. The catalyst was used as a cathode material in Na-O_2 cell and it showed 6.7 fold specific capacity as CNF. This enhancement is attributed to the synergistic effect of high electronically conductive CNF core and RuO_2-Mn_2O_3 shell,

as well as the novel 3D morphology of the composite. The more exposed edges and uniform distribution of RuO_2 nano-particles in RuO_2/Mn_2O_3/CNF is due to the trapping effect of Mn_2O_3 nano-rods, which is confirmed by TEM and SEM results.

Bibliography

[1] A. Sieminski, "International energy outlook," *Energy Information Administration (EIA)*, vol. 28, no. 7, pp. 1037 – 1050, 2014.

[2] L. J. H. P. G. Bruce, S. A. Freunberger and J.-M. Tarascon, "Li-o2 and li-s batteries with high energy storage," *Nature Materials*, vol. 11, no. 1, pp. 19–29, 2012.

[3] M. C. K.-M. X. L. D. C. J. P. L. Z. Yang, J. Zhang and J. Liu, "Electrochemical energy storage for green grid," *Chemical reviews*, vol. 11, no. 5, pp. 3577–3613, 2011.

[4] M. Whittingham, "Chemistry of intercalation compounds: Metal guests in chalcogenide hosts," *Progress in Solid State Chemistry*, vol. 12, no. 1, pp. 41 – 99, 1978.

[5] K. Mizushima, P. Jones, P. Wiseman, and J. Goodenough, "Lixcoo2 (0¡x¡-1): A new cathode material for batteries of high energy density," *Materials Research Bulletin*, vol. 15, no. 6, pp. 783 – 789, 1980.

[6] G. Girishkumar, B. McCloskey, A. C. Luntz, S. Swanson, and W. Wilcke, "Lithium air battery: Promise and challenges," *The Journal of Physical Chemistry Letters*, vol. 1, no. 14, pp. 2193–2203, 2010.

[7] J.-S. Lee, S. Tai Kim, R. Cao, N.-S. Choi, M. Liu, K. T. Lee, and J. Cho, "Metal–air batteries with high energy density: Li–air versus zn–air," *Advanced Energy Materials*, vol. 1, no. 1, pp. 34–50, 2011.

[8] P. Adelhelm, P. Hartmann, C. L. Bender, M. Busche, C. Eufinger, and J. Janek, "From lithium to sodium: cell chemistry of room temperature sodium–air and sodium–sulfur batteries," *Beilstein Journal of Nanotechnology*, vol. 6, pp. 1016–1055, 2015.

[9] K. F. Blurton and A. F. Sammells, "Metal/air batteries: Their status and potential — a review," *Journal of Power Sources*, vol. 4, no. 4, pp. 263 – 279, 1979.

[10] K. Abraham and Z. Jiang, "A polymer electrolyte-based rechargeable lithium/oxygen battery," *Journal of The Electrochemical Society*, vol. 143, no. 1, pp. 5–9, 1996.

[11] T. Ogasawara, A. Débart, M. Holzapfel, P. Novák, and P. G. Bruce, "Rechargeable li2o2 electrode for lithium batteries," *Journal of the American Chemical Society*, vol. 128, no. 4, pp. 1390–1393, 2006. PMID: 16433559.

[12] P. Hartmann, C. L. Bender, M. Vračar, A. K. Dürr, A. Garsuch, J. Janek, and P. Adelhelm, "A rechargeable room-temperature sodium superoxide (nao2) battery," *Nat Mater*, vol. 12, pp. 228–232, 03 2013.

[13] Z. Ma, X. Yuan, L. Li, Z.-F. Ma, D. P. Wilkinson, L. Zhang, and J. Zhang, "A review of cathode materials and structures for rechargeable lithium-air batteries," *Energy Environ. Sci.*, vol. 8, pp. 2144–2198, 2015.

[14] M. H. J. Zheng, R. Liang and E. Plichta, "Theoretical energy density of li–air batteries," *Journal of The Electrochemical Society*, vol. 155, no. 6, pp. A432–A437, 2008.

[15] X.-h. Yang and Y.-y. Xia, "The effect of oxygen pressures on the electrochemical profile of lithium/oxygen battery," *Journal of Solid State Electrochemistry*, vol. 14, p. 109, Feb 2009.

[16] N. T. A. G. S. Meini, M. Piana and H. A. Gasteiger, "The effect of water on the discharge capacity of a non-catalyzed carbon cathode for li-o2 batteries," *Electrochemical and Solid-State Letters*, no. 4, pp. A45–A48, 2012.

[17] B. D. McCloskey, R. Scheffler, A. Speidel, D. S. Bethune, R. M. Shelby, and A. C. Luntz, "On the efficacy of electrocatalysis in nonaqueous li–o2 batteries," *Journal of the American Chemical Society*, vol. 133, no. 45, pp. 18038–18041, 2011. PMID: 21995529.

[18] Y.-C. Lu, D. G. Kwabi, K. P. C. Yao, J. R. Harding, J. Zhou, L. Zuin, and Y. Shao-Horn, "The discharge rate capability of rechargeable li-o2 batteries," *Energy Environ. Sci.*, vol. 4, pp. 2999–3007, 2011.

[19] J. Kim, H. Park, B. Lee, W. M. Seong, H.-D. Lim, Y. Bae, H. Kim, W. K. Kim, K. H. Ryu, and K. Kang, "Dissolution and ionization of sodium superoxide in sodium–oxygen batteries," vol. 7, pp. 10670 EP –, 02 2016.

[20] S. Kang, Y. Mo, S. P. Ong, and G. Ceder, "Nanoscale stabilization of sodium oxides: Implications for na–o2 batteries," *Nano Letters*, vol. 14, no. 2, pp. 1016–1020, 2014. PMID: 24417743.

[21] Q. Sun, H. Yadegari, M. N. Banis, J. Liu, B. Xiao, X. Li, C. Langford, R. Li, and X. Sun, "Toward a sodium–"air" battery: Revealing the critical role of humidity," *The Journal of Physical Chemistry C*, vol. 119, no. 24, pp. 13433–13441, 2015.

[22] B. D. McCloskey, J. M. Garcia, and A. C. Luntz, "Chemical and electrochemical differences in nonaqueous li–o2 and na–o2 batteries," *The Journal of Physical Chemistry Letters*, vol. 5, no. 7, pp. 1230–1235, 2014. PMID: 26274476.

[23] P. Hartmann, M. Heinemann, C. L. Bender, K. Graf, R.-P. Baumann, P. Adelhelm, C. Heiliger, and J. Janek, "Discharge and charge reaction paths in sodium–oxygen batteries: Does nao2 form by direct electrochemical growth or by precipitation from solution?," *The Journal of Physical Chemistry C*, vol. 119, no. 40, pp. 22778–22786, 2015.

[24] J. E. Nichols and B. D. McCloskey, "The sudden death phenomena in nonaqueous na–o2 batteries," *The Journal of Physical Chemistry C*, vol. 121, no. 1, pp. 85–96, 2017.

[25] S. Y. Sayed, K. P. C. Yao, D. G. Kwabi, T. P. Batcho, C. V. Amanchukwu, S. Feng, C. V. Thompson, and Y. Shao-Horn, "Revealing instability and irreversibility in nonaqueous sodium-o2 battery chemistry," *Chem. Commun.*, vol. 52, pp. 9691–9694, 2016.

[26] T. Liu, G. Kim, M. T. L. Casford, and C. P. Grey, "Mechanistic insights into the challenges of cycling a nonaqueous na–o2 battery," *The Journal of Physical Chemistry Letters*, vol. 7, no. 23, pp. 4841–4846, 2016. PMID: 27934035.

[27] Z. E. M. Reeve, C. J. Franko, K. J. Harris, H. Yadegari, X. Sun, and G. R. Goward, "Detection of electrochemical reaction products from the sodium–oxygen cell with solid-state 23na nmr spectroscopy," *Journal of the American Chemical Society*, vol. 139, no. 2, pp. 595–598, 2017. PMID: 28004929.

[28] I. Landa-Medrano, R. Pinedo, X. Bi, I. Ruiz de Larramendi, L. Lezama, J. Janek, K. Amine, J. Lu, and T. Rojo, "New insights into the instability of discharge products in na–o2 batteries," *ACS Applied Materials & Interfaces*, vol. 8, no. 31, pp. 20120–20127, 2016. PMID: 27447935.

[29] S. Xu, S. Lau, and L. A. Archer, "Co2 and ambient air in metal-oxygen batteries: steps towards reality," *Inorg. Chem. Front.*, vol. 2, pp. 1070–1079, 2015.

[30] D. G. Kwabi, T. P. Batcho, C. V. Amanchukwu, N. Ortiz-Vitoriano, P. Hammond, C. V. Thompson, and Y. Shao-Horn, "Chemical instability of dimethyl sulfoxide in lithium–air batteries," *The Journal of Physical Chemistry Letters*, vol. 5, no. 16, pp. 2850–2856, 2014. PMID: 26278088.

[31] R. Black, S. H. Oh, J.-H. Lee, T. Yim, B. Adams, and L. F. Nazar, "Screening for superoxide reactivity in li-o2 batteries: Effect on li2o2/lioh crystallization," *Journal of the American Chemical Society*, vol. 134, no. 6, pp. 2902–2905, 2012. PMID: 22283803.

[32] N. Zhao and X. Guo, "Cell chemistry of sodium–oxygen batteries with various nonaqueous electrolytes," *The Journal of Physical Chemistry C*, vol. 119, no. 45, pp. 25319–25326, 2015.

[33] L. Lutz, D. Alves Dalla Corte, M. Tang, E. Salager, M. Deschamps, A. Grimaud, L. Johnson, P. G. Bruce, and J.-M. Tarascon, "Role of electrolyte anions in the na–o2 battery: Implications for nao2 solvation and the stability of the sodium solid electrolyte interphase in glyme ethers," *Chemistry of Materials*, vol. 29, no. 14, pp. 6066–6075, 2017.

[34] I. I. Abate, L. E. Thompson, H.-C. Kim, and N. B. Aetukuri, "Robust nao2 electrochemistry in aprotic na–o2 batteries employing ethereal electrolytes with a protic additive," *The Journal of Physical Chemistry Letters*, vol. 7, no. 12, pp. 2164–2169, 2016. PMID: 27214400.

[35] D. Capsoni, M. Bini, S. Ferrari, E. Quartarone, and P. Mustarelli, "Recent advances in the development of li–air batteries," *Journal of Power Sources*, vol. 220, no. Supplement C, pp. 253 – 263, 2012.

[36] S. Monaco, F. Soavi, and M. Mastragostino, "Role of oxygen mass transport in rechargeable li/o2 batteries operating with ionic liquids," *The Journal of Physical Chemistry Letters*, vol. 4, no. 9, pp. 1379–1382, 2013. PMID: 26282288.

[37] J. Wang, Y. Li, and X. Sun, "Challenges and opportunities of nanostructured materials for aprotic rechargeable lithium–air batteries," *Nano Energy*, vol. 2, no. 4, pp. 443 – 467, 2013.

[38] L. Jin, L. Xu, C. Morein, C.-h. Chen, M. Lai, S. Dharmarathna, A. Dobley, and S. L. Suib, "Titanium containing gamma-mno2 hollow spheres: One-step synthesis and catalytic activities in li/air batteries and oxidative chemical reactions," *Advanced Functional Materials*, vol. 20, no. 19, pp. 3373–3382, 2010.

[39] T. T. Truong, Y. Liu, Y. Ren, L. Trahey, and Y. Sun, "Morphological and crystalline evolution of nanostructured mno2 and its application in lithium–air batteries," *ACS Nano*, vol. 6, no. 9, pp. 8067–8077, 2012. PMID: 22866870.

[40] M. Endo, C. Kim, K. Nishimura, T. Fujino, and K. Miyashita, "Recent

development of carbon materials for li ion batteries," *Carbon*, vol. 38, no. 2, pp. 183 – 197, 2000.

[41] S. Sharma and B. G. Pollet, "Support materials for pemfc and dmfc electrocatalysts—a review," *Journal of Power Sources*, vol. 208, no. Supplement C, pp. 96 – 119, 2012.

[42] Y. Shao, S. Park, J. Xiao, J.-G. Zhang, Y. Wang, and J. Liu, "Electrocatalysts for nonaqueous lithium–air batteries: Status, challenges, and perspective," *ACS Catalysis*, vol. 2, no. 5, pp. 844–857, 2012.

[43] Y. Lei, J. Lu, X. Luo, T. Wu, P. Du, X. Zhang, Y. Ren, J. Wen, D. J. Miller, J. T. Miller, Y.-K. Sun, J. W. Elam, and K. Amine, "Synthesis of porous carbon supported palladium nanoparticle catalysts by atomic layer deposition: Application for rechargeable lithium–o2 battery," *Nano Letters*, vol. 13, no. 9, pp. 4182–4189, 2013. PMID: 23927754.

[44] W. X. D. W. R. E. W. J. L. J. Xiao, D. Wang and J.-G. Zhang, "Optimization of air electrode for li/air batteries," *ournal of The Electrochemical Society*, no. 4, pp. A487–A492, 2010.

[45] J. Z. D. W. W. Xu, J. Xiao and J.-G. Zhang, "Optimization of nonaqueous electrolytes for primary lithium/air batteries operated in ambi- ent environment," *Journal of the Electrochemical Society*, vol. 156, no. 10, pp. A773–A779, 2009.

[46] Q. Li, R. Cao, J. Cho, and G. Wu, "Nanostructured carbon-based cathode catalysts for nonaqueous lithium-oxygen batteries," *Phys. Chem. Chem. Phys.*, vol. 16, pp. 13568–13582, 2014.

[47] H. Yadegari, C. J. Franko, M. N. Banis, Q. Sun, R. Li, G. R. Goward, and X. Sun, "How to control the discharge products in na–o2 cells: Direct evidence toward the role of functional groups at the air electrode surface," *The Journal of Physical Chemistry Letters*, vol. 8, no. 19, pp. 4794–4800, 2017. PMID: 28926257.

[48] N. Ortiz-Vitoriano, T. P. Batcho, D. G. Kwabi, B. Han, N. Pour, K. P. C. Yao, C. V. Thompson, and Y. Shao-Horn, "Rate-dependent nucleation and growth of nao2 in na–o2 batteries," *The Journal of Physical Chemistry Letters*, vol. 6, no. 13, pp. 2636–2643, 2015. PMID: 26266746.

[49] E. Yilmaz, C. Yogi, K. Yamanaka, T. Ohta, and H. R. Byon, "Promoting formation of noncrystalline li2o2 in the li–o2 battery with ruo2 nanoparticles," *Nano Letters*, vol. 13, no. 10, pp. 4679–4684, 2013. PMID: 24024674.

[50] R. A. Wong, A. Dutta, C. Yang, K. Yamanaka, T. Ohta, A. Nakao, K. Waki, and H. R. Byon, "Structurally tuning li2o2 by controlling the surface properties of carbon electrodes: Implications for li–o2 batteries," *Chemistry of Materials*, vol. 28, no. 21, pp. 8006–8015, 2016.

[51] C. Yang, R. A. Wong, M. Hong, K. Yamanaka, T. Ohta, and H. R. Byon, "Unexpected li2o2 film growth on carbon nanotube electrodes with ceo2 nanoparticles in li–o2 batteries," *Nano Letters*, vol. 16, no. 5, pp. 2969–2974, 2016. PMID: 27105122.

[52] Y. Cui, Z. Wen, and Y. Liu, "A free-standing-type design for cathodes of rechargeable li-o2 batteries," *Energy Environ. Sci.*, vol. 4, pp. 4727–4734, 2011.

[53] H. Cheng and K. Scott, "Selection of oxygen reduction catalysts for rechargeable lithium–air batteries—metal or oxide?," *Applied Catalysis B: Environmental*, vol. 108-109, no. Supplement C, pp. 140 – 151, 2011.

[54] M. M. Thackeray, M. K. Y. Chan, L. Trahey, S. Kirklin, and C. Wolverton, "Vision for designing high-energy, hybrid li ion/li–o2 cells," *The Journal of Physical Chemistry Letters*, vol. 4, no. 21, pp. 3607–3611, 2013.

[55] A. Débart, J. Bao, G. Armstrong, and P. G. Bruce, "An o2 cathode for rechargeable lithium batteries: The effect of a catalyst," *Journal of Power Sources*, vol. 174, no. 2, pp. 1177 – 1182, 2007. 13th International Meeting on Lithium Batteries.

[56] A. Riaz, K.-N. Jung, W. Chang, S.-B. Lee, T.-H. Lim, S.-J. Park, R.-H. Song, S. Yoon, K.-H. Shin, and J.-W. Lee, "Carbon-free cobalt oxide cathodes with tunable nanoarchitectures for rechargeable lithium-oxygen batteries," *Chem. Commun.*, vol. 49, pp. 5984–5986, 2013.

[57] W.-W. Yin and Z.-W. Fu, "A highly efficient bifunctional heterogeneous catalyst for morphological control of discharged products in na-air batteries," *Chem. Commun.*, vol. 53, pp. 1522–1525, 2017.

[58] Q. Sun, J. Liu, X. Li, B. Wang, H. Yadegari, A. Lushington, M. N. Banis, Y. Zhao, W. Xiao, N. Chen, J. Wang, T.-K. Sham, and X. Sun, "Atomic layer deposited non-noble metal oxide catalyst for sodium–air batteries: Tuning the morphologies and compositions of discharge product," *Advanced Functional Materials*, vol. 27, no. 16, pp. 1606662–n/a, 2017. 1606662.

[59] H. Yadegari, M. Norouzi Banis, A. Lushington, Q. Sun, R. Li, T.-K. Sham, and X. Sun, "A bifunctional solid state catalyst with enhanced cycling stability for na and li-o2 cells: revealing the role of solid state catalysts," *Energy Environ. Sci.*, vol. 10, pp. 286–295, 2017.

[60] F. Wu, Y. Xing, J. Lai, X. Zhang, Y. Ye, J. Qian, L. Li, and R. Chen, "Micrometer-sized ruo2 catalysts contributing to formation of amorphous na-deficient sodium peroxide in na–o2 batteries," *Advanced Functional Materials*, vol. 27, no. 30, pp. 1700632–n/a, 2017. 1700632.

[61] E. A. Paoli, F. Masini, R. Frydendal, D. Deiana, C. Schlaup, M. Malizia, T. W. Hansen, S. Horch, I. E. L. Stephens, and I. Chorkendorff, "Oxygen evolution on well-characterized mass-selected ru and ruo2 nanoparticles," *Chem. Sci.*, vol. 6, pp. 190–196, 2015.

[62] D. J. Morgan, "Resolving ruthenium: Xps studies of common ruthenium materials," *Surface and Interface Analysis*, vol. 47, no. 11, pp. 1072–1079, 2015. SIA-15-0179.R1.

[63] Y. K. Kim and H. Park, "Light-harvesting multi-walled carbon nanotubes and cds hybrids: Application to photocatalytic hydrogen production from water," *Energy Environ. Sci.*, vol. 4, pp. 685–694, 2011.

[64] P. Balaya, H. Li, L. Kienle, and J. Maier, "Fully reversible homogeneous and heterogeneous li storage in ruo2 with high capacity," *Advanced Functional Materials*, vol. 13, no. 8, pp. 621–625, 2003.

[65] N. Zhao, C. Li, and X. Guo, "Long-life na-o2 batteries with high energy efficiency enabled by electrochemically splitting nao2 at a low overpotential," *Phys. Chem. Chem. Phys.*, vol. 16, pp. 15646–15652, 2014.

[66] W.-J. Kwak, Z. Chen, C. S. Yoon, J.-K. Lee, K. Amine, and Y.-K. Sun, "Nanoconfinement of low-conductivity products in rechargeable sodium–air batteries," *Nano Energy*, vol. 12, no. Supplement C, pp. 123 – 130, 2015.

[67] R. Black, A. Shyamsunder, P. Adeli, D. Kundu, G. K. Murphy, and L. F. Nazar, "The nature and impact of side reactions in glyme-based sodium–oxygen batteries," *ChemSusChem*, vol. 9, no. 14, pp. 1795–1803, 2016.

[68] J. Huang, B. Zhang, Z. Bai, R. Guo, Z.-L. Xu, Z. Sadighi, L. Qin, T.-Y. Zhang, G. Chen, B. Huang, and J.-K. Kim, "Anomalous enhancement of li-o2 battery performance with li2o2 films assisted by nifeox nanofiber catalysts: Insights into morphology control," *Advanced Functional Materials*, vol. 26, no. 45, pp. 8290–8299, 2016.

[69] J. S. Lee, C. Lee, J. Jun, D. H. Shin, and J. Jang, "A metal-oxide nanofiber-decorated three-dimensional graphene hybrid nanostructured flexible electrode for high-capacity electrochemical capacitors," *J. Mater. Chem. A*, vol. 2, pp. 11922–11929, 2014.

[70] Y. Luo, Y.-Q. Deng, W. Mao, X.-J. Yang, K. Zhu, J. Xu, and Y.-F. Han, "Probing the surface structure of alpha-mn2o3 nanocrystals during co oxidation by operando raman spectroscopy," *The Journal of Physical Chemistry C*, vol. 116, no. 39, pp. 20975–20981, 2012.

[71] S. Mar, C. Chen, Y. Huang, and K. Tiong, "Characterization of ruo2 thin films by raman spectroscopy," *Applied Surface Science*, vol. 90, no. 4, pp. 497 – 504, 1995.

[72] Y. Yang, T. Zhang, X. Wang, L. Chen, N. Wu, W. Liu, H. Lu, L. Xiao, L. Fu, and L. Zhuang, "Tuning the morphology and crystal structure of li2o2: A graphene model electrode study for li–o2 battery," *ACS Applied Materials & Interfaces*, vol. 8, no. 33, pp. 21350–21357, 2016. PMID: 27459128.

[73] Y. Yang, W. Liu, N. Wu, X. Wang, T. Zhang, L. Chen, R. Zeng, Y. Wang, J. Lu, L. Fu, L. Xiao, and L. Zhuang, "Tuning the morphology of li2o2 by noble and 3d metals: A planar model electrode study for li–o2 battery," *ACS Applied Materials & Interfaces*, vol. 9, no. 23, pp. 19800–19806, 2017. PMID: 28537386.